University of South Bohemia in České Budějovice

Faculty of Science

Molecular modeling of biomolecules – surface interactions

Ph.D. Thesis

Ing. Ondřej Kroutil

Supervisor: doc. RNDr. Milan Předota, Ph.D.

Faculty of Science, Institute of Physics and Biophysics,
University of South Bohemia in České Budějovice

České Budějovice 2016

Annotation

Interactions between (bio)molecules, ions and solid surfaces play crucial role in many biological processes as well as in many scientific applications and understanding of this phenomenon on *molecular level* is a challenging task for today science. Computer simulations can provide detailed view on atomic level if carefully prepared and evaluated models are used.

In this thesis, interactions of several types of (bio)molecules with inorganic surfaces are studied by classical and ab initio molecular dynamics. Chemisorbed biomolecules, namely DNA and oligopeptide, covalently attached to graphene and mercury surface, respectively, were studied to make link with DNA chip design and experimental label-free electrochemical measurements, respectively. Quartz (101) surface model applicable to wide range of pH conditions was developed and evaluated against experimental X-ray data. Physisorption of the nucleobases on quartz (101) surface and oxalate dianion on rutile (110) was examined and discussed.

Declaration [in Czech]

Prohlašuji, že svoji disertační práci jsem vypracoval samostatně pouze s použitím pramenů a literatury uvedených v seznamu citované literatury.

Prohlašuji, že v souladu s § 47b zákona č. 111/1998 Sb. v platném znění souhlasím se zveřejněním své disertační práce, a to v úpravě vzniklé vypuštěním vyznačených částí archivovaných Přírodovědeckou fakultou elektronickou cestou ve veřejně přístupné části databáze STAG provozované Jihočeskou univerzitou v Českých Budějovicích na jejích internetových stránkách, a to se zachováním mého autorského práva k odevzdanému textu této kvalifikační práce. Souhlasím dále s tím, aby toutéž elektronickou cestou byly v souladu s uvedeným ustanovením zákona č. 111/1998 Sb. zveřejněny posudky školitele a oponentů práce i záznam o průběhu a výsledku obhajoby kvalifikační práce. Rovněž souhlasím s porovnáním textu mé kvalifikační práce s databází kvalifikačních prací Theses.cz provozovanou Národním registrem vysokoškolských kvalifikačních prací a systémem na odhalování plagiátů.

České Budějovice, 26. 6. 2016

………………………………….

Ondřej Kroutil

This thesis originated from research projects solved at Faculty of Science, University of South Bohemia.

Přírodovědecká
fakulta
Faculty
of Science

Financial support

Acknowledgements

List of papers and author's contribution

The presented thesis is based on the papers OK1-OK4. Although publications OK5 and OK6 fall under the biophysical modeling as previous ones, the topic is different and thus they are not included in this thesis. Numbering OK1-OK4 will be used throughout this thesis.

OK1) Kroutil O., Chval Z., Skelton A. A., Předota M. (2015): Computer Simulations of Quartz (101)–Water Interface over a Range of pH Values. The Journal of Physical Chemistry C 119 (17), 9274-9286; IF(2014) = 4.772
OK implemented new force field to Gromacs software package, performed all molecular dynamics simulations of water and ions interacting with the quartz surface and carried out all analyses. He participated in the paper writing.

OK2) Kabeláč M., **Kroutil O.**, Předota M., Lankaš F., Šíp M. (2012): Influence of a charged graphene surface on the orientation and conformation of covalently attached oligonucleotides: a molecular dynamics study. Physical Chemistry Chemical Physics 14 (12), 4217-4229; IF(2014) = 4.493
OK prepared the model of graphene and attached oligonucleotide, performed several molecular dynamics simulations and participated in the paper writing.

OK3) Dorčák V., Kabeláč M., **Kroutil O.**, Bednářová K. and Vacek J. (2016): Electrocatalytic Monitoring of Peptidic Proton-Wires. (Manuscript accepted in Analyst); IF(2014) = 4.107
OK participated in the paper writing.

OK4) Kroutil O., Minofar B., Kabeláč M. (2015): Structure and Dynamics of Solvated Hydrogenoxalate and Oxalate Anions: a Theoretical Study, (Manuscript)
OK prepared all models, performed all ab initio molecular dynamics simulations and did several analyses. He participated in the paper writing.

OK5) Kroutil O., Romancová I., Šíp M., Chval Z. (2014): Cy3 and Cy5 Dyes Terminally Attached to 5'C End of DNA: Structure, Dynamics, and Energetics. The Journal of Physical Chemistry B 118 (47), 13564-13572; IF(2014) = 3.302
OK prepared all models, performed several molecular dynamics simulations and did several analyses. He participated in the paper writing.

OK6) Kroutil O., Předota M., Chval Z. (2016): Pt…Hw Non-Classical Interaction in Water Dissolved Pt(II)-Complexes: Coaction of Electronic Effects with Solvent-Assisted Stabilization., Inorg Chem, 55 (7), 3252–3264; IF(2014) = 4.762
OK prepared all models for ab inito molecular dynamics, performed dynamics simulations and did several analyses. He participated in the paper writing.

Contents

List of abbreviations:

AIMD	Ab Initio Molecular Dynamics
BOMD	Born-Oppenheimer Molecular Dynamics
CMD	Classical Molecular Dynamics
CPMD	Car-Parinello Molecular Dynamics
GPW	Gaussian Plane-Wave method
MD	Molecular Dynamics
RDF	Radial Distribution Function
RESP	Restrained ElectroStatic Potential
AA	Amino Acid
Cx	Oxalate carbon
DIW	DeIonized Water
ds-DNA	double-stranded Deoxyribonucleic Acid
HIE	neutral histidine
HIP	protonated histidine
Hw	Water hydrogen
Ow	Water oxygen
Ox	Oxalate oxygen
ox-1	Hydrogenoxalate anion
ox-2	Oxalate dianion
ss-DNA	single-stranded Deoxyribonucleic Acid
AFM	Atomic Force Microscopy
BL	Brandt and Lyubartsev parameters
CPS	Current chronoPotentiometric Stripping
CPU	Central Processing Unit
CTR	Crystal Truncation Rod
EDL	Electric Double-Layer
GPU	Graphical Processor Unit
CHER	Catalytic Hydrogen Evolution Reaction
MA	Matsui and Akaogi parameters
MUSIC-CD	MUltiSIte Complexation – Charge Distribution
PZC	Point of Zero Charge
RAXR	Resonant Anomalous X-ray Reflectivity
SHG	Second Harmonic Generation
SPR	Surface Plasmon Resonance
XR	X-ray Reflectivity
XSW	Standing Wave

1. Introduction

1.1 Motivation

Interactions between (bio)molecules, ions and solid surfaces play crucial role in many biological processes as well as in many scientific applications. Understanding of this phenomenon on *molecular level* is a challenging task for today science. From the beginning of the 20th century when Langmuir presented his model for the monolayer adsorption of species onto simple surfaces [Langmuir, 1918], the surface and interface science has gone long journey and has grown up into fully-fledged discipline with its own specific experimental methods and theoretical models. Experimental techniques like atomic force microscopy (AFM), surface plasmon resonance (SPR), resonant anomalous X-ray reflectivity (RAXR) and second harmonic generation (SHG) together with in-silico techniques like classical molecular dynamics (CMD), ab initio molecular dynamics (AIMD), and accompanied by various models of electric double-layer (EDL) and surface complexation models (e.g. MUSIC-CD, i.e. MUltiSIte Complexation – Charge Distribution) can give complex and detailed picture of what happens at the surface and interface during adsorption of (almost) any kind atom, ion or molecule.

(Bio)molecules/solid surface interactions that are heart of this thesis belong to a wide family of processes generally called *adsorption*. Adsorption is defined as "the accumulation of a substance at an interface" [Butt, 2003] and it is purely surface phenomenon with no penetration of the *adsorbate* into the bulk region of the *adsorbent* (contrary to *absorption*). *Interface* is a narrow contact region between two phases where

physical and chemical properties of adsorbate differ from their bulk values. Properties and processes in this region are crucial for understanding of adsorption.

If we consider three states of matter, i.e. solid, liquid and gas state, we get several combinations of the interfaces: the solid–liquid, the solid–gas, and the liquid–gas interface (commonly called *surfaces*), or interfaces between two immiscible liquids (liquid–liquid interfaces) or different solid materials (solid–solid interfaces). Out of these combinations, only the *solid–liquid* interface is a subject of our interest, because all simulations described in this thesis are tightly connected to experiments investigating this interface.

Adsorption can be categorized using various criteria, but the strength of the interaction between adsorbate and adsorbent is the key factor. Weak adsorption where only van der Waals forces act between surface and adsorbate is called *physisorption* while strong adsorption accompanied by creation and/or disruption of chemical bonds is called *chemisorption*. Physisorption is usually characterized by the sorption energy of the order of 20–40 kJ.mol^{-1}, relatively free adsorbate able to diffuse and rotate on the surface, and quick establishing of an adsorption equilibrium. Contrary, chemisorption has usually typical sorption energies of 100–400 kJ.mol^{-1}, the adsorbate is relatively immobile and usually does not diffuse on the surface and often leads to surface reconstruction. We have dealt with both types of the adsorption in our work, physisorption is described in Chapter 3 and chemisorption in Chapter 4.

As adsorption of (bio)molecules takes place very often in water environment with dissolved ions, one has to be also beware of adsorption of these substances. Water molecules at a solid substrate often experience a hindered rotation relative to those in the bulk, forming dense layers of the solvent up to few nanometers above the surface. Then, if liberated from the surface via displacement by an adsorbed molecule, a net entropy gain results. At the same time ions can occupy charged spots on the surface and/or and adsorbent, hereby influencing equilibrium of the adsorption. Thus, high-quality models of the surfaces and adsorbing molecules that properly quantify interactions with water and ions are crucial for the success of simulations. Development and evaluation of these models is discussed in detail in Chapter 2 and Chapter 3.

Due to complexity of the topic and corresponding large number of simulations, systems and analyzed data, not all results included in thesis have been published yet. But to give overall picture of our work and to maintain hierarchy of the topic, we combine both published and unpublished data in the following text.

1.2 Organic molecules, nucleic acids and peptides

1.2.1 Oxalic acid

Oxalic acid is the most simple dicarboxylic acid, being composed of two COOH groups directly connected together (see Figure 1-1, $C_2H_2O_4$). It occurs in nature as a calcium oxalate mineral (whewellite, weddellite), it has been spotted in traces in atmosphere as a product of the combustion of fossil fuels or exhaust of cars, representing 37-69 % of the total dicarboxylic acids in atmosphere [Kawamura and Ikushima, 1993]. It also shows a wide biological activity in plants and animals. For example, it was revealed [Sharma, 1993] that oxalic acid and diacylglycerol metabolites in blood are quantitatively depleted under sleep-restricted conditions and restored after recovery of sleep. Under physiological conditions, oxalate ion can interact with calcium ion and thus it plays an important role in the formation of calcium-containing uroliths in human body. It has high solubility (143 $g.dm^{-3}$; due to polarity and formation of intra and intermolecular hydrogen bonds) and very low first deprotonation constant of pK_{a1} = 1.24. Thus, in near-neutral pH it occurs mainly as oxalate dianion ($C_2O_4^{2-}$) with very small amounts as hydrogenoxalate anion ($C_2HO_4^-$, pK_{a2} = 4.23) (Figure 1-1). Albeit oxalic acid and both its anions are relatively simple chemical compounds, their structure, solvation and parameterization is still a matter of debate.

Figure 1-1. Fraction of total oxalate in any protonation form as a function of pH. Neutral pH highlighted by dashed curve. Inset: corresponding structures and naming.

1.2.2 Nucleobases

Nucleic acid bases, i.e. nitrogenous purine and pyrimidine bases, and their related structures with attached 5-membered sugar ring and phosphate group(s) - nucleosides and nucleotides (see Figure 1-3 in Charter 1.2.3), are essential molecules for all living beings. They serve as building blocks of nucleic acids and as co-factors of enzymatic reactions (coenzyme A, FAD, FMN), and alone they participate in metabolism as chemical energy

storage media, or in cellular signaling [Francis and Corbin, 1999]. Nucleosides are also used as dietary supplements and modified forms of purines and pyrimidines are promising new drugs [Jordheim, 2013].

The primary nucleobases are cytosine (DNA and RNA), guanine (DNA and RNA), adenine (DNA and RNA), thymine (DNA) and uracil (RNA), abbreviated as C, G, A, T, and U, respectively (Figure 1-2, uracil not shown). Adenine and guanine belong to the purine and thymine, cytosine and uracil to the pyrimidine family of bases. Apart primary nucleobases also modified versions exist with hypoxanthine, 7-methylguanine, or 5-hydroxymethyl cytosine being the most known examples.

Immobilization of nucleobases (and all derived molecules mentioned above) onto inorganic surfaces is a determining factor for many scientific techniques such as biosensing (DNA microarray) [OK2], chromatographic and electrophoretic separation of these species [Marrubini, 2010], oligonucleotide synthesis (phosphoramidite process) [Sanghvi, 2000], for development of biocompatible materials [Li, 2011] and for prebiotic polymerization of RNAs and DNAs [Brindley, 1968; Mignon, 2009].
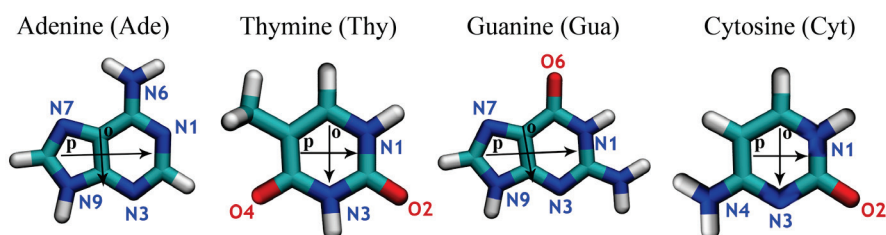
Figure 1-2. Four nucleobases used in our study. Main atoms and vectors used to complete bivariate plots shown.

There is an ongoing interest in nucleobases adsorption onto various surfaces. The most recent experimental studies have focused mainly on the adsorption onto pure metal [Feyer, 2011; Plekan, 2010] (and especially gold [Pagliai, 2012; Plekan, 2012; Yang, 2009; Kundu, 2009]) and carbon-based [Panigrahi, 2012; Varghese, 2009; Sowerby, 2001] surfaces due to applicability of these results in biosensing. The main emphasis in these studies has been on the orientation of the adsorbed molecules (perpendicular vs. parallel) and a type of the adsorption (physi- vs. chemisorption). Similar situation occurs in the field of theoretical chemistry with several quantum mechanical [Bogdan and Morari, 2012; Umadevi and Sastry, 2011; Rajarajeswari, 2011; Piana and Bilic, 2006] and molecular dynamic studies [Maleki, 2011; Rapino, 2005; Piana and Bilic, 2006].

Some experimental studies have focused on the behavior of the nucleic acids components near metal-oxides [Cleaves, 2010; Plekan, 2007] and clay materials [Baú, 2012; Carneiro 2011] with the main motivation to explain a prebiotic chemical processes, since it is believed that immobilization of nucleic acid components is a necessary step for the polymerization of these species.

Few molecular dynamics studies have tried to identify a binding arrangement and to quantify the strength of interactions of nucleobases with the rutile surface [Monti, 2011] and with a Si (111) surface with attached alkyl-amine molecules [Monti, 2011].

To the best of our knowledge, there are no systematic all-atom molecular dynamics simulations studying these nucleobases binding on various surfaces at various conditions.

1.2.3 Nucleic acids

Nucleic acid molecules (NAs) are essential biomolecules that all living organisms have in common. They execute variety of functions in living cells ranging from transmission of genetic information between generations and transcription of the genetic information into proteins, through catalytic functions to gene regulation. Basic structural unit of nucleic acids is the nucleotide (Figure 1-3a, yellow), each of which contains a pentose sugar (deoxyribose in DNA and ribose in RNA), a phosphate group, and a nucleobase (Figure 1-3b). Sugar and phosphate group creates so-called sugar-phosphate backbone (Figure 1-3a, purple) that carries large negative charge due to deprotonated phosphate (PO_4^{-1}) groups. Nucleobases were described in detail in previous chapter (Chapter 1.2.2). NAs can be either single-stranded or double-stranded with complementary bases that can *hybridize* via
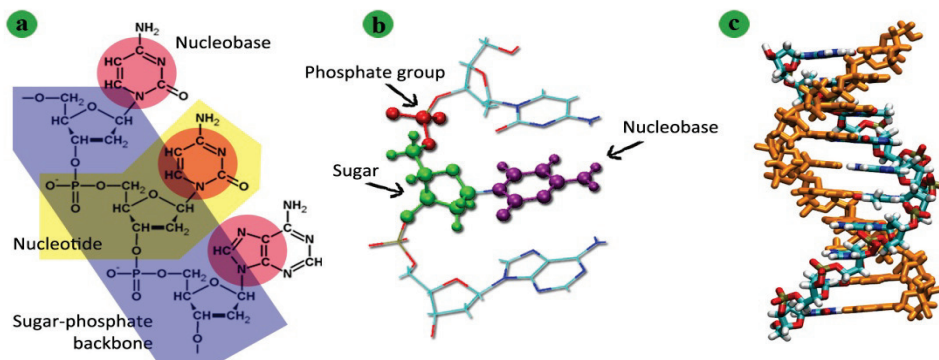

Figure 1-3. (a) Schematic representation of the DNA constituents, (b) Ball-and-stick representation of the nucleotide; (c) Licorice representation of a double stranded DNA with its typical helical geometry. Single strand highlighted by orange color.

making of the weak hydrogen bonds between nucleotides and forming typical double-stranded helix. DNA molecules are in most cases double-stranded, whereas RNA molecules are usually single-stranded [Hodge, 2009].

DNA is more stable than RNA and is located in a cell nucleus where it stores genetic information, being coiled into higher structural units called *chromosomes*. All chromosomes together make up so-called *genome* that is, in the case of humans, composed of approximately 3 billion of base pairs arranged into 46 chromosomes. *Gene* is a certain part of long DNA molecule that encodes a functional RNA or protein product. Rapid and cheap detection of a sequence of the nucleotides in a gene (so-called *sequencing*), is a main interest of today science because with knowledge of the exact order of nucleotides one can identify changes in genes, associations with diseases and phenotypes, study how different organisms are related and how they evolved, determine if there is risk of genetic diseases, etc.

For this purpose, microarrays or DNA chips are appropriate devices. Arrays of tens to tens of thousands of microscopic spots containing single-stranded deoxyribonucleotides are attached to a solid surface (such as a membrane, a polymer, or glass) of the microarray, and these are used to analyze simultaneously a sample solution containing fragments of nucleic acids. Oligonucleotides (capture probes) in individual spots are identical, but their sequences are different for each spot to match the various complementary DNA sequences (targets) present in a given sample. The sequences of surface-immobilized capture probes needs to be designed to meet several criteria: they should not allow the formation of internal structures such as hairpins and they should be sensitive to sequence variations and bind only to complementary strands. Usually, software tools available for probe design during the process of microarray development are based on standard hybridization conditions, i.e. nucleic acids in solution, not being attached to a surface.

However, the surface plays an important role and can influence process of hybridization to a large extent. First, the capture probes are immobilized to a certain extent by surface binding and therefore their molecular dynamics is different from that describing a system of two free strands in a solution. Second, the presence of the surface and the interactions of the capture probe with the surface represent an important sterical hindrance making single-strand – double-strand transitions more difficult. Third, in addition to the van der Waals interactions, the surface, whether it is charged or not, generates nontrivial electrostatics and interfacial structure owing to the interactions between the solution and the surface, influencing the density profiles of the water and ions in the vicinity of the surface and attached probes.

1.2.4 Peptides

Peptides are short chains composed of amino acid monomers (Figure 1-4a) linked by peptide bonds. There is 23 proteinogenic, i.e. protein-building amino acids. Peptide bonds are formed by condensation reaction when the carboxyl group of one amino acid reacts with the amine group of another (Figure 1-4b) while water is released. As peptides are a continuous and unbranched chain (Figure 1-4c), they fall under the broad chemical classes of biological oligomers and polymers, alongside nucleic acids, oligosaccharides and polysaccharides. Peptides contain approximately 50 or fewer amino acids, but the border is not strict.
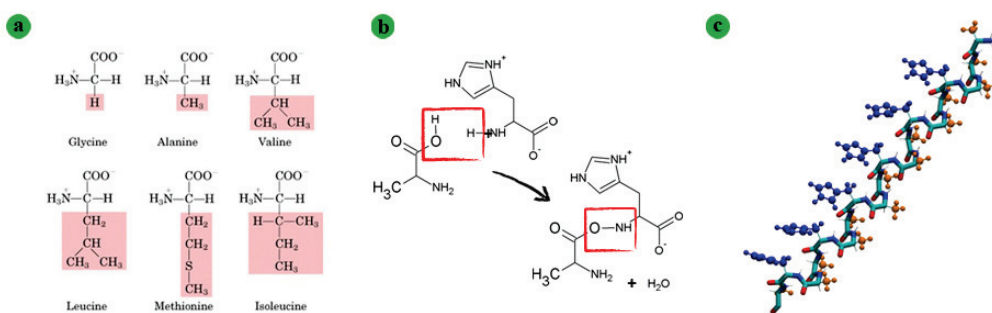

Figure 1-4. (a) Example of the several amino acids with highlighted side functional groups, (b) Creation of the peptide bond; (c) Peptide chain, backbone in licorice representation, side functional groups highlighted by orange and blue color and ball-and-sticks representation.

Similarly as in a label-free or label based analysis of nucleic acid (and also of polysaccharides and glycans), so far only carbon and mercury based electrodes have been found useful for the sensitive analysis required by contemporary peptide/protein research [Paleček, 2012; Paleček, 2015]. Use of carbon electrodes is limited to oxidation reactions of tyrosine (Tyr) or tryptophan (Trp) residues, while utilization of mercury or amalgam electrodes was earlier restricted only to the reduction processes involving SH- groups of Cys and/or SS-bonds of cystine (CSSC) residues. Nowadays, considerable progress in development of a method called constant current chronopotentiometric stripping (CPS), that utilizes mercury electrode, has widened number of amino acids that can be detected by this type of an electrode (see below), and has allowed characterization of the nanomolar quantities of various peptides and proteins.

This *label-free* and also *structure-sensitive* method is based on catalytic hydrogen evolution reaction (CHER) with a typical analytical output known as *peak H* (Figure 1-5)
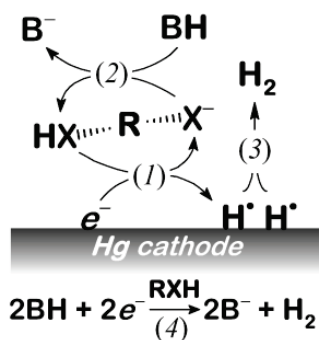
Figure 1-5. CHER mechanism

[Heyrovsky, 2005]. In hydrogen evolution catalyzed by a peptide or a protein molecule, CPS peak H is reflecting consumption of electrons in the irreversible reduction of exchangeable protons from the functional groups (–XH, located at side chains of some AA residues) close to the negatively charged electrode surface (reaction *1*, Figure 1-5). The effect is much more pronounced in buffered media in which the catalyst (peptide or protein) molecule (R–XH/R–X⁻) in adsorbed state mediates a transport of protons from the acid constituent of a buffer (BH, reaction *2*) onto negatively charged electrode surface where subsequently surface bound hydrogen atoms (H$^\bullet$) combine into more stable molecules of gaseous hydrogen (H$_2$, reaction *3*). Deprotonated functional groups (–X⁻) are then immediately reprotonated by an excess of slightly acidic BH (reaction *2*) and enter reaction *1* closing thus a catalytic cycle. The net result is that while the catalyst is restored, the acid constituent of the solution is reduced under formation of molecular hydrogen (reaction *4*).

Artificial and bioactive peptides were studied mostly as a protein like models to identify catalytically active sites or to better understand fundamental basis of the electrocatalytic process taking place in the case of complex protein molecules [Sestáková, 2000; Enache 2013; Zuman, 2005]. In search for catalytically active amino acid residues, so far involvement of Cys thiol (pKa ~ 8), lysine (Lys) ε-ammonium (pKa ~ 11), arginine (Arg) guanidinium (pKa ~ 12), and His imidazolium (pKa ~ 6) groups had been unambiguously confirmed [Zuman, 2005, Palecek, 2014]. However, also ammonium group (pKa ~ 9) at peptidic chain N-end and hydroxyl group at Ser, Tyr, or Thr residues (pKa ~ 10) are capable of proton exchange reaction in solution but their involvement in CHER was neither confirmed nor denied.

From previous brief description of the CPS method it is evident, that interactions and conformations of peptide(s) on a mercury electrode are crucial for success of this method. Contrary to previous successful event, it was also shown on a set of angiotensin (AT) peptides [Dorčák, 2013] that presence of aspartic acid (Asp) residue bearing negatively charged carboxylate group in the vicinity of Arg residue can *cancel* catalytic activity of the peptide. Other preliminary results from Dorčák group with several Cys containing peptides indicate that also carboxylate group at side chain of glutamic acid (Glu) residue or at C-end of the peptide backbone can prevent involvement of the SH-groups in CHER. It is believed that very probably the electrostatic repulsion between the negative charges at

the electrode surface and carboxylate group prevailed over the electrostatic attraction of the positively charged Arg guanidinium group or hydrophobic interaction of Cys SH group and thus, detracted their involvement in CHER.

1.3   Computer simulations

1.3.1   Classical molecular dynamics

The classical molecular dynamics simulations propagate a series of instantaneous atomic configuration over time by integration of Newton's equations of motion. In CMD the atoms are represented by interacting sites (points) corresponding to their nuclei, while the electrons are considered only effectively via partial charges located at the atomic or auxiliary sites and assumed to follow the Born-Oppenheimer approximation. With this significant simplification and adopting pair-wise potentials for all inter-atomic interactions except angular bonded terms, systems composed of $\sim 10^5$ atoms can be simulated for times up to hundreds of nanoseconds on modern clusters of CPU and GPU units.

Basics of the classical molecular dynamics can be found elsewhere [Leach, 2001; Schlick, 2002]. For the purpose of this thesis just brief description of the non-bonded interactions is mentioned because we had to take special care of them.

Non-bonded interactions play an important role in MD simulations, because precisely these interactions stand behind adsorption phenomena, higher-level structure of molecules, hydration and hydrogen-bonding. Therefore the best possible parameters describing non-bonded interactions are crucial for success of the simulation.

We explicitly incorporate two types of non-bonded interactions in MD simulations: electrostatic interactions that are described by Coulomb's law (Equation 1-1):

$$U_{Elst.}(r_{ij}) = \frac{q_i q_j}{4\pi\varepsilon_0 r_{ij}} \tag{1-1}$$

and van der Waals forces that are almost exclusively described by Lennard-Jones potential (Equation 1-2) in standard biomolecular force fields:

$$U_{LJ}(r_{ij}) = 4\varepsilon_{ij}\left[\left(\frac{\sigma_{ij}}{r_{ij}}\right)^{12} - \left(\frac{\sigma_{ij}}{r_{ij}}\right)^6\right] \tag{1-2}$$

where σ_{ij} denotes the distance where the intermolecular potential between two atoms is zero, and and ε_{ij} the well depth characterizing how strong the attraction between two

atoms is. Using Lorentz-Berthelot combination rule (Equation 1-3) one can derive the cross parameters for different species:

$$\sigma_{ij} = \frac{\sigma_{ii}+\sigma_{jj}}{2}; \ \varepsilon_{ij} = \sqrt{\varepsilon_{ii}\varepsilon_{jj}} \tag{1-3}$$

Another possibility is to take into account van der Waals forces in simulation using Buckingham potential (also known as exp-6 potential) (Equation 1-4):

$$U_{BH}(r_{ij}) = A_{ij}\exp\left(-\frac{r_{ij}}{b_{ij}}\right) - C_{ij}r_{ij}^6 \tag{1-4}$$

where A_{ij}, b_{ij} describe components of the repulsive interaction and C_{ij} describes the attractive interaction. Both potentials for van der Waals interactions appeared in our work together in Chapter 2.4 and we had to dealt with their incompatibility.

1.3.2 Ab initio molecular dynamics

Unlike classical molecular dynamics, in ab initio molecular dynamics forces are computed on-the-fly by accurate electronic structure calculations and therefore AIMD does not rely on a set of empirical parameters as CMD. It also implies that bond making and breaking events are naturally included when ab initio calculations are involved.

Two approaches are in use [Vidossich, 2016]: Born-Oppenheimer MD (BOMD) where the time-independent electronic structure problem is solved for the actual nuclear configuration at each step during the dynamics, and Car-Parrinello MD (CPMD) where the electronic orbitals are evolved together with the ions, thus not requiring optimization of the wave function at each MD step.

Computer power requirements of ab initio calculations are enormous. State-of-art AIMD calculations dealt with systems composed of hundreds of atoms and simulation times up to hundreds of picoseconds, i.e. several orders of magnitude less than CMD.

In our work [OK4], we have used BOMD to study conformation and solvation shell of the oxalic acid anions.

1.3.3 Structural characteristics

Radial distribution function

The key structural property, radial distribution function $g(r)$, gives the probability of finding a particle in the distance r from another particle. Simply speaking, radial

distribution function (RDF) informs us how atoms in a system are radially packed around each other. This is particularly useful if one wants to describe the structure of disordered molecular systems, especially pure liquids and solutions. The disordered movement of molecules and atoms in a system with hardly recognizable order is converted by computing RDF to behavior of the average structure. It can reveal short range order due to presence of hydrogen bonds, London forces, etc., including contributions from nearest neighbors as well as more distant molecules.

RDF $g_{AB}(r)$ between particles of type A and B, resp. A and A is computed as (Equation 1-5):

$$g_{AB}(r) = \frac{N_{AB}(r, \Delta r)}{N_A N_B \dfrac{4\pi r^2 \Delta r}{V}}; \quad g_{AA}(r) = \frac{N_{AA}(r, \Delta r)}{\dfrac{N_A(N_A - 1)}{2} \dfrac{4\pi r^2 \Delta r}{V}}$$

(1-5)

where N_{AA}, resp. N_{AB} is the number of corresponding pairs within a spherical shell of thickness Δr and centered around distance r from one of the species and N_A, N_B are numbers of particles (atoms) of given kind.

Except of being very informative structural property, great benefit of RDF arises from the fact, that it can be indirectly determined via its relation with the structure factor $S(q)$ from neutron scattering or X-ray scattering data. This allows experimental measurements and computer simulations to be mutually compared and interpreted.

Axial density profiles

Axial density profiles represent density profiles of species averaged laterally in the x and y directions to obtain only z dependent density, where z axis is perpendicular to the surface, typically with origin at the interface and facing the liquid phase. They are useful for the analysis of the distribution of groups or atoms across the interface including recognition of dissolved vs adsorbed species. They are easily accessible from the simulations and more indirectly from experimental studies too. Comparison between theoretical and experimental data was done by us many times [OK1, Chapter 2.1, Předota *et al.*, 2004] and allowed us to justify our models and thereafter broaden experimental findings with more detailed molecular view.

From the experimental techniques, X-ray reflectivity (XR), crystal truncation rod (CTR) and standing wave (XSW) measurements provide invaluable information on the structure of interfacial liquid (most commonly water), surface relaxation, and geometry of adsorbed ions [Zhang, 2004]. Typical XR signal, $R(Q)$, of quartz (101) in contact with deionized water and RbCl solution as a function of vertical momentum transfer is depicted
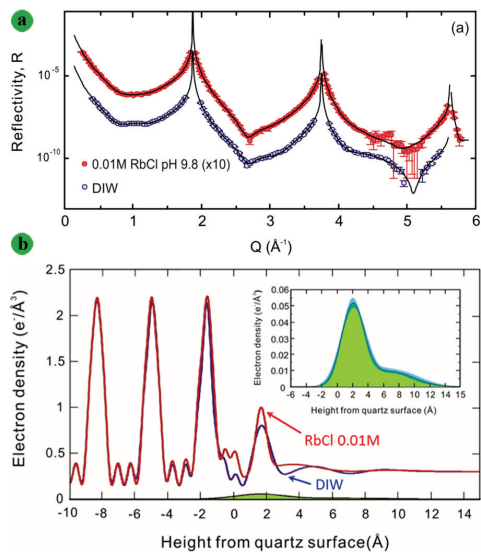
at Figure 1-6a [Bellucci, 2015], accompanied with derived axial electron density profiles (Figure 1-6b).

Figure 1-6. (a) Specular XR signal, $R(Q)$, of quartz (101) in contact with DIW (empty blue circles), and RbCl solution 0.01 M at pH 9.8 (fullred circles), as a function of vertical momentum transfer, Q;.(b) Derived electron density profiles for quartz(101) in contact with DIW (blue line) and 0.01 M RbCl solution at pH 9.8 (red line).

2. Surfaces

Four different surfaces have appeared one by one in our studies, namely graphene, mercury, quartz (101) and rutile (110) surfaces (Figure 2-1). This chapter describes in depth developing, evaluation and comparison of these surface models.

2.1 Graphene

Graphene surface was used as a substrate in our study focusing on a behavior of nucleic acids chemisorbed on the graphene surface [OK2].

Graphene is two-dimensional material only one monolayer thick (Figure 2-1). It can be considered as one layer from multi-layered graphite mineral. It consists of carbon atoms densely packed in regular hexagonal pattern with surface atom density of 38.2 atoms.nm^{-2}.
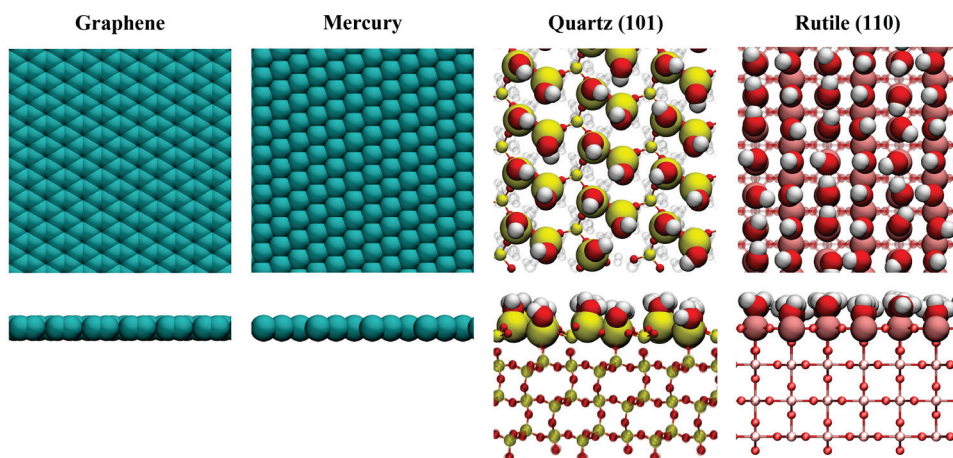

Figure 2-1. Top and side views of four different surfaces used in our studies.

This surface atom density is more than four times the density of mercury atoms used to model mercury surface. Graphene surface possesses very extraordinary properties like very high specific surface area (2630 m^2.g^{-1}), remarkable electron mobility at room temperature (15000 cm^2.V^{-1}.s^{-1}), unique optical properties with an unexpectedly high opacity, etc.

This particular surface was selected as the substrate in our simulations, because it was a relatively simple but realistic surface with its geometry independent of pH, salt concentration, etc. Furthermore, some theoretical studies on DNA interactions with carbon nanotubes (surfaces based on graphene geometry) were available at that time and binding of DNA to carbon nanotubes was identified as a way to open the door to carbon–nanotube–based applications in biotechnology.

For the carbon atoms of graphene, we have used 'CA' atomic type from Amber99SB force field with parameters σ_{CC} = 0.340 nm and ε_{CC} = 0.360 kJ.mol^{-1}. Similar parameters were used in other papers simulating carbon–nanotube–DNA interactions [Hummer, 2001; Zhao, 2007; Johnson, 2009].
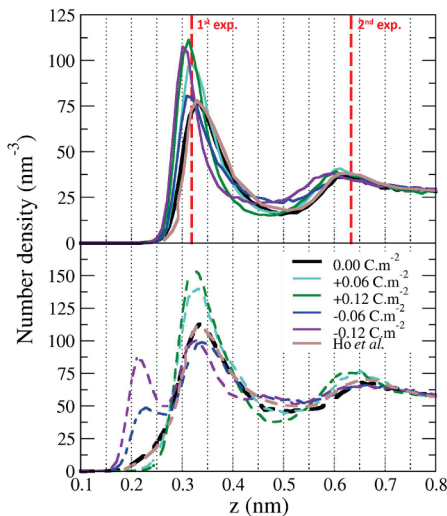

Figure 2-2. Axial density profiles of water oxygen Ow (upper graph) and hydrogen Hw (lower graph) for all surface charge densities. Positions of experimentally observed density peaks for water are shown by red dashed lines [Ho, 2013].

Axial density profiles of the water oxygens and hydrogens depicted in Figure 2-2 were not included in the original manuscript, but for comparison it is worthwhile to discuss them here. On water oxygen profile, two distinct peaks up to cca 1 nm above the surface are visible. In uncharged system, the first peak is positioned at 0.333 nm and the second one at 0.625 nm. In their experimental and theoretical study, Zhou et al. [Zhou, 2012] have derived from X-ray measurements positions of the first and second peak of the water to be 0.319 and 0.633 nm above the graphene surface. Thus, our results are just 0.015 and 0.008 nm off the experimental ones. With increasing positive surface charge, position of the first peak uniformly moves toward the surface and its height increase considerably. This is caused by increased

electrostatic attraction between positive surface charge and negative partial charge on the oxygen. Influence of the negative surface charges on oxygen density profile is different. While for surface charge density -0.06 C.m^{-2} the change is rather small with respect to neutral system, for surface charge density -0.12 C.m^{-2} height of the first peak reaches similar values as for +0.12 C.m^{-2}.

Water hydrogen profile shows two peaks at 0.334 and 0.664 nm above the uncharged surface. The first peak is positioned at the same distance as water oxygen. Since our axial density profiles have practically the same shape as those in the study by Ho *et al.* [Ho, 2013] (Figure 2-2), we suppose that even in our simulations some of the water molecules within the first hydration layer (~9 %) point one of their OH bonds towards the surface, others having planar geometry with both hydrogens parallel to the surface. Positive surface charge density changes position of the first peak in accordance with the change of the position of the oxygen first peak. Contrary, negative charge density causes more pronounced changes. Negative surface charge attracts positively charged hydrogens and these having no assigned Lennard-Jones parameters start to orient toward the surface with no restriction on how close they can get to the surface. This behavior is represented by peaks emerging at ~0.22 nm above the surface.

2.2 Mercury

Mercury served as an electrode in combined experimental and ab initio study by Dorčák *et al.* (see Chapter 1.2.4) [OK3], whose results were further developed in classic molecular dynamics (CMD) study (Chapter 4.2).

Since mercury is the only common metal which is liquid at ordinary temperatures,

Table 2-1. Lennard-Jones parameters from available mercury models. Final parameters used in our simulations are highlighted by green color.

Ref.	σ_{Hg} (nm)	ε_{Hg} (kJ.mol^{-1})	Parametrization on
Hg0[1]	-	-	Water next to the liquid/solid mercury **benchmark**
Hg1[2]	0.2610	11.10	Liquid bulk mercury
Hg2[3]	0.2969	6.23	Free diffusion of Hg^{2+} in water
Hg3[4]	0.3128	4.04	Hg^0 dimer

[1]Hg0 ref. [Dimitrov and Raev, 2000; Bopp and Heinzinger 1998], [2]Hg1 ref. [Bomont and Bretonnet, 2006], [3]Hg2 ref. [Kuss, 2009] and [4]Hg3 ref. [Munro, 2001].
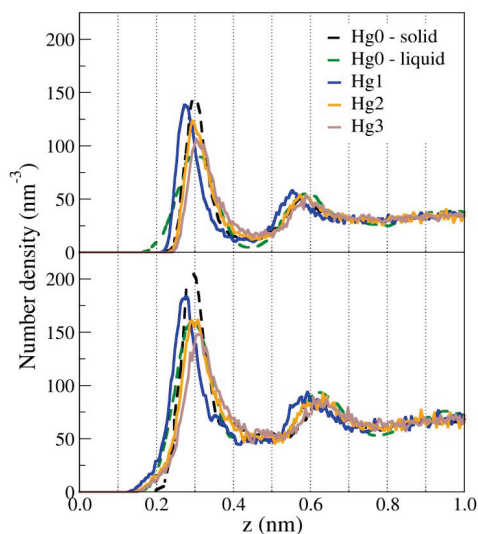
Figure 2-3. Axial number density profiles of water oxygen (top) and hydrogen (bottom) above the mercury surface. Hg0 - solid and liquid represent the benchmark data.

computer simulations of this element based on empirical methods are not easy. Lack of studies is not surprising and only few of them describe mercury using functions which are compatible with biological force fields [Bomont and Bretonnet, 2006; Kuss, 2009; Munro, 2001]. The Lennard-Jones parameters obtained from these works are summarized in Table 2-1. Unfortunately, none of these parameters was parameterized in a study of interactions with biomolecules. Thus, a reproduction of the axial water density profile on mercury was used as a criterion of reliability of the parameters. Results obtained from computer simulations based on ab initio data [Dimitrov and Raev, 2000; Bopp and Heinzinger 1998; noted as Hg0] served for us as a benchmark.

It is clear from the Figure 2-3 that the density profiles are rather insensitive to the choice of Lennard-Jones parameters, however slight differences in positions and heights of peaks can be found. The Hg2 parameters were selected for our further study due to the best reproducibility of ab initio data. The rigid solid mercury surface was used systematically in all our simulations. It was shown by Bosio *et al.* [Bosio, 1979] and Porter and Zinn [Porter and Zinn, 1993] that liquid mercury surface is smooth down to the atomic level with average Hg-Hg distance very close to the distance found in bulk mercury (appr. 3.0 Å), and can be approximated by a solid α-mercury lattice. The final surface atom density of mercury surface was 11.7 atoms.nm^{-2}.

2.3   Quartz (101)

Quartz surface was extensively studied by us [OK1] and new partial charges that extend original ClayFF force field [Cygan, 2004] to be able to describe deprotonated surfaces were presented in our study.

Silicon dioxide with all its crystalline and amorphous modifications is one of the most abundant materials of Earth's crust. α-quartz (α-SiO$_2$) is a crystalline form of silicon dioxide, which can be found in soils, clays, and rocks and constitute about 20% of the Earth's exposed crust. α-SiO$_2$ is very important for environmental applications as well as for mimicking laboratory experiments (e.g. oligonucleotides or other molecules attached to glass surface).

Quartz surface exposed to water is covered with rather strongly acidic hydroxyl groups, silanols, that become partially deprotonated above the point of zero charge. It has been suggested that the pH$_{pzc}$ at the point of zero charge (PZC) for quartz is approximately 2.0−4.5 (Figure 2-4). As the pH is increased, the number of deprotonated silanols and the negative charge of the surface increase and the properties of the surface and the interface change considerably.
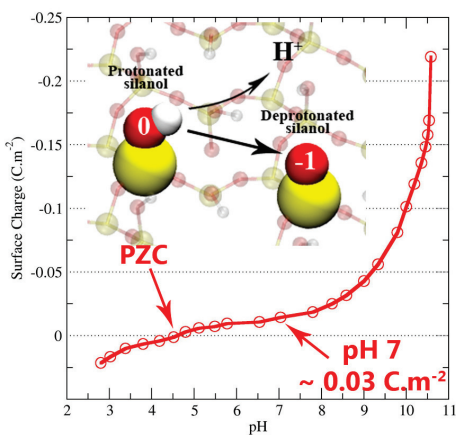

Figure 2-4. Charging curve of the α-quartz surface. Inset: scheme of the deprotonation reaction.

From this point of view it was rather surprising, that for neutral crystalline and amorphous forms of SiO$_2$ there were several force fields available, whereas force fields that incorporate deprotonated silanol groups were rare [Hassanali, 2010; Butenuth, 2012; Emami, 2014]. Moreover, some of these force fields used terms that were incompatible with common biomolecular force fields (see also Chapter 2.4) and hardly implementable to standard simulation packages like Gromacs or Amber.

For this reason we modified the well established ClayFF force field to be able to model charged quartz surfaces properly. Based on ab initio cluster calculations, we proposed method how to redistribute remaining partial charge after deprotonation and we have tested our new modification against experimental data. Results were quite encouraging, giving good agreement between simulation and experiment in positions of the water and ions above the charged surface. The availability of the modified force field allowed us to carry out much more realistic simulations of quartz compared to existing models of neutral surface (see Chapter 3.2)

2.4 Rutile (110)

Rutile (110) surface was extensively studied by Předota *et al.* in series of papers that have focused on water behavior at the rutile interface [Předota, 2004], ions at the rutile interface [Předota, 2004] and viscosity and diffusivity measurements at the rutile interface [Předota, 2007].

Matsui and Akaogi (MA) parameters [Matsui and Akaogi, 1991] (originally developed to model bulk properties of TiO_2) have been used by Předota for a rutile/water interface in combination with SPC/E water model [Berendsen, 1987]. It was proved, that MA model gives very good agreement with the experimental data, although originally derived for different application. Unfortunately, MA parameters are unsuitable for simulations in standard MD packages (Gromacs, Amber, Charmm) in combination with standard force fields for (bio)molecules. The reason is Buckingham potential (Equation 1-4) used in MA model to describe van der Waals interaction between Ti and O atoms of the surface. Unfortunately, biomolecular force fields use almost exclusively Lennard-Jones potential (Equation 1-2) to describe van der Waals forces and combination of both potentials is extremely demanding in terms of computation time and preparation of the cross interaction tables. At least two publications [Brandt and Lyubartsev, 2015; Luan, 2015] have dealt with this problem and have tried to fit MA parameters with Lennard-Jones potential.

Table 2-2 shows that at the end both studies have reached similar values of ε and σ parameters and shapes of fitting Lennard-Jones curves match original Buckingham potentials with similar accuracy. None of the mentioned studies has focused on rutile (110) albeit it was shown [Fenter, 2000] that this crystallographic face is the most abundant in nature. For that reason we had to test these new fitting parameters and

Table 2-2. Buckingham potential parameters and Lennard-Jones potential parameters for titanium and oxygen atoms in

	Matsui-Akaogi[1]			Brandt-Lyubartsev[2]		Luan-Huynh-Zhou[3]	
	A (kJ.mol)$^{-1}$	b (Å)	C (kJ.mol^{-1}.Å^{-6})	σ (nm)	ε (kJ.mol^{-1})	σ (nm)	ε (kJ.mol^{-1})
Ti-Ti	3002664	0.154	506	0.1958	2.542	0.1960	2.427
O-O	1136872	0.234	2916	0.2875	1.390	0.2887	1.297
Ti-O	1636167	0.194	1215	0.2417	1.880	0.2423	1.774

[1] ref. [Matsui and Akaogi, 1991], [2] ref. [Brandt and Lyubartsev, 2015], [3] ref. [Luan, 2015]
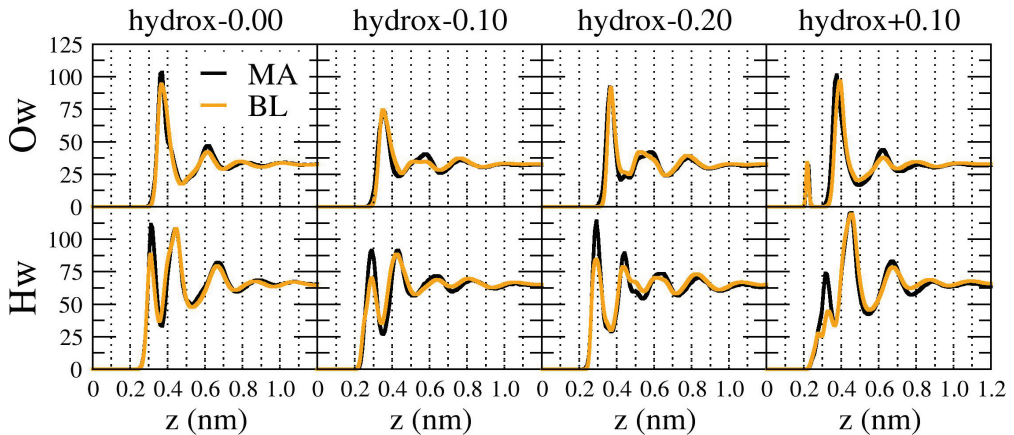
Figure 2-5. Comparison of the water oxygen (top) and hydrogen (bottom) axial density profiles extracted from simulations with Matsui-Akaogi parameters (black lines) and Brandt and Lyubartsev parameters (orange lines). Hydroxylated TiO_2 (110) surfaces with surface charge densities 0.00, -0.10, -0.20 and +0.10 $C.m^{-2}$ were used as substrates.

compare new results with those using original MA model. Due to complexity of the published data, we have decided to test parameters of Brandt and Lyubartsev (BL) [Brandt and Lyubartsev, 2015].

Figure 2-5 shows water oxygen and hydrogen axial density profiles at the TiO_2 (110) surfaces with various surface charge densities. Comparison of original data from Předota *et al.* [Předota, 2004a; Předota, 2004b] and new data based on Brandt and Lyubartsev fit indicates that for oxygen, satisfactory agreement is obtained. In all systems, second peaks are slightly lower with BL and the one in the system with positive surface charge is shifted by 0.02 nm to higher values. Water hydrogen distribution is more sensitive to the choice of potentials. First peaks are lower with BL, indicating somewhat different orientation of water molecules in the first adsorbed layer.

Distributions of sodium and chloride ions were compared too (Figure 2-6). Sodium ions give good agreement between original and fitted parameters, however height of the peaks is slightly lower with BL. Although not so important for the systems with negative surface charges (notice the different vertical scales in Figure 2-6), differences in distributions of chloride ions for the original and fitted parameters are greater. First peaks are underpopulated with BL while second peaks are higher with BL than with MA. The same holds true for second and third peaks in the system with positive surface charge,
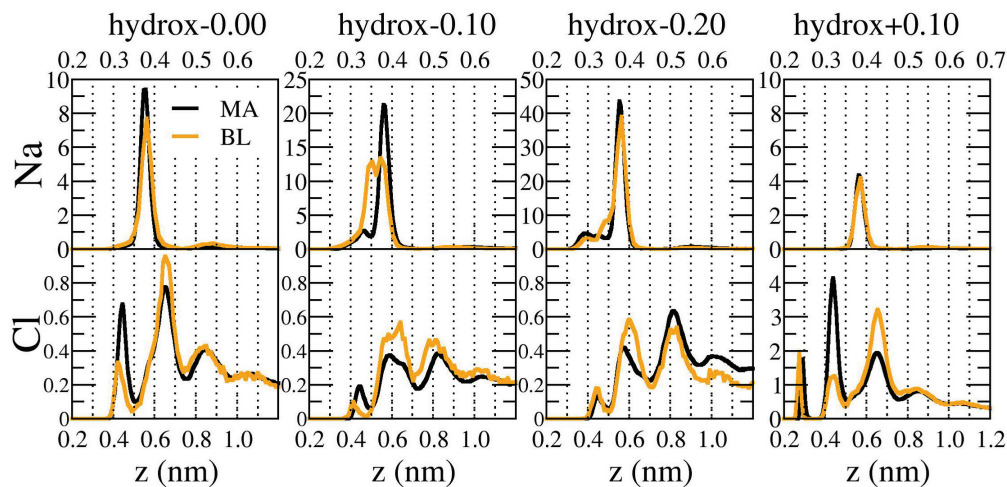
Figure 2-6. Comparison of the sodium (top) and chloride (bottom) axial density profiles from simulations with Matsui-Akaogi parameters (black lines) and Brandt and Lyubartsev parameters (orange lines). Hydroxylated TiO_2 (110) surfaces with surface charge densities 0.00, -0.10, -0.20 and +0.10 C.m^{-2} were used as substrates. Note different x and y scales.

while positions and heights of the first peaks are comparable for both sets of parameters used.

It is clear that simulations with new parameters slightly differ from those with original Matsui-Akaogi parameters. New parameters slightly underestimate strength of the non-bonded interactions giving less populated first peaks, mainly for water hydrogen and chloride. On the other hand, simulations with new parameters result in very similar results for water oxygen and sodium ions. Despite these deviations, both force fields comparably well agree with experimental data, where available. Because of advantages of using Lennard-Jones potential with Brandt and Lyubartsev parameters for studying interactions with standardly parameterized molecules, we have used these fit parameters in consequent study on oxalate adsorption on rutile surface (for oxalate parameterization see Chapter 3.1).

2.5 Discussion

Due to their similarities and differences, it is worthwhile to draw a comparison between graphene and mercury surfaces and, similarly, between quartz and rutile surfaces. All the studied surfaces have in common exploration of the effect of electrostatics on the behavior of liquid phase including ions and molecules present, namely surface charge or applied voltage in a simulation cell. As mentioned previously, on the metal oxide surfaces charging naturally arises from deprotonation of the surface hydroxyl groups. On metal/metalloid surfaces, charging can be realized by putting partial charge on surface atoms (used in the case of graphene) or by switching up electric field in a simulation cell (used in the case of mercury). All used surface charge densities and corresponding electric fields are summarized in Table 2-3. We used Equation 2-1 to relate surface charge density with electric field:

$$\sigma = E\varepsilon_0 \tag{2-1}$$

where σ is surface charge density in $C.m^{-2}$, E is electric field in $V.m^{-1}$ and ε_0 is permittivity of vacuum.

2.5.1 Graphene vs. mercury

Graphene and mercury surfaces were used as monoatomic layers in our simulations. While in the graphene case carbon atoms were held together by bond and angle potentials, in the mercury case the initial α-mercury lattice was kept frozen during simulations and mercury atoms were treated as solid Lennard-Jones spheres. Final Lennard-Jones

Table 2-3. Surface charge densities σ and electric field intensities E used in simulations with different surfaces. Similar surface charge densities are highlighted by orange and blue color, respectively.

Graphene		Mercury		Quartz (101)		Rutile (110)	
σ ($C.m^{-2}$)	E ($V.nm^{-1}$)	σ ($C.m^{-2}$)	E ($V.nm^{-1}$)	σ ($C.m^{-2}$)	E ($V.nm^{-1}$)	σ ($C.m^{-2}$)	E ($V.nm^{-1}$)
0.000	0.00	0.000	0.00	0.000	0.00	0.000	0.00
±0.059	3.33	±0.001	±0.14	-0.030	-1.69	0.100	5.65
±0.118	6.66	±0.011	±1.25	-0.060	-3.39	-0.100	-5.65
±0.297	16.77	±0.030	±3.45	-0.120	-6.78	-0.200	-11.29
±0.594	33.54	±0.061	±6.89			-0.400	-22.59

parameters for graphene carbon atoms were σ_{CC} = 0.340 nm, ε_{CC} = 0.360 kJ.mol^{-1}, and σ_{Hg} = 0.2969 nm, ε_{Hg} = 6.23 kJ.mol^{-1} for mercury atoms.

The differences in σ and ε parameters as well as differences in surface charging reflect in behavior of water at the studied surfaces (Figure 2-7). In uncharged systems, water is closer to mercury surface by 0.033 nm compared to graphene. Situation is the same for both oxygen and hydrogen. On mercury surface, the peaks are higher, indicating greater water structuring. Non-zero surface charge reduce the difference in positions and heights of the peaks between graphene and mercury surface. Interestingly, despite different charging method both surfaces give similarly pronounced small peak around ~0.22 nm on Hw axial density profile.

2.5.2 Quartz vs. rutile

Both surfaces have some characteristics in common: surface hydroxyl groups, charging via partial deprotonation of these groups and several types of the hydroxyl groups. Surface number density of the hydroxyl groups on quartz and rutile is 5.8 and 10.4 OH.nm^{-2}, respectively, i.e. rutile surface carries almost two times more hydroxyl groups on its surface.

To quantify the adsorption, we plot in Figure 2-8 the dependence of the amount of adsorbed ions (considering inner-sphere adsorption and first peak of outer-sphere adsorption) on surface charge density for both quartz (101) and (110) rutile surfaces
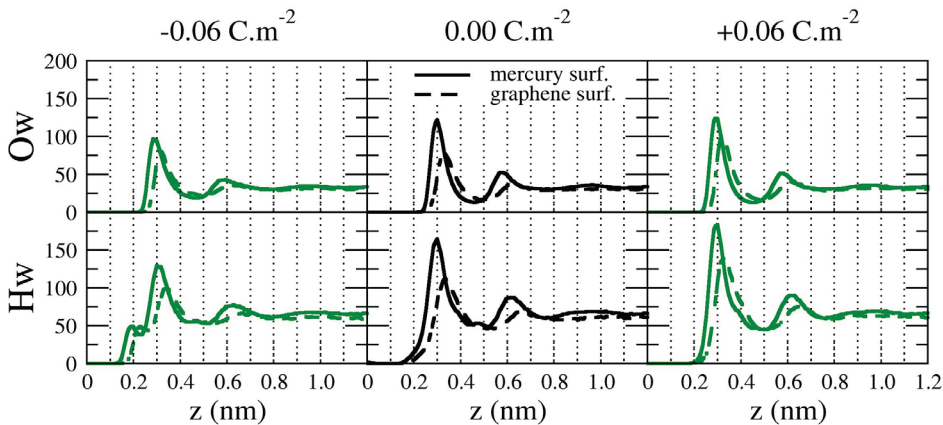

Figure 2-7. Comparison of the water oxygen (top) and hydrogen (bottom) axial density profiles on mercury (full line) and graphene (dashed line) surfaces with various surface charge densities.
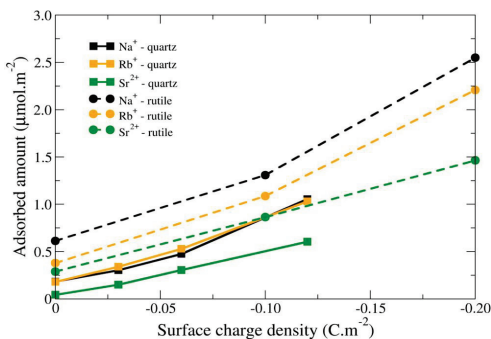
Figure 2-8. Dependence of the adsorbed amount of sodium (black), rubidium (orange), and strontium (green) ions on surface charge density. Data for rutile (dashed lines) surface are taken from Table 8 of Předota *et al.* [Předota, 2013]

[Předota, 2013]. Adsorption on rutile is stronger compared to quartz for all ions. Differences are bigger for neutral surfaces where the rutile surface adsorbs 3.3, 2.1, and 6.6 times more sodium, rubidium, and strontium ions, respectively, than the quartz surface. With increasing surface charge density these ratios decrease. Rutile has higher selectivity to different ion species, with Na^+ adsorption being larger than that of Rb^+ and Sr^{2+} on all surfaces. On quartz, the adsorption of sodium and rubidium is practically the same, but the adsorption of Sr^{2+} is much lower, particularly on the neutral surface. The experimental value of adsorbed rubidium on quartz in the first two adsorption layers is 0.23 ± 0.03 Rb/A_{UC} (where $A_{UC} = 0.338$ nm^2 is the area of a unit cell along the (101) plane) [Bellucci, 2015]. Our simulations predict a value of 0.20 Rb/A_{UC} when integrating over the first two well-pronounced peaks or 0.24 Rb/A_{UC} if even the third peak (up to 0.93 nm from the surface) is taken into account.

3. Physisorption of organic molecules and nucleobases

3.1 Oxalic acid parameterization

Unlike standard biomolecular residues (e.g. amino acids, DNA nucleotides, carbohydrates, etc.), small organic molecules have to be parametrized prior to use in simulations. As we witnessed, this step can be non-trivial. Unsuitable bonding parameters together with inappropriately-optimized partial charges and Lennard-Jones parameters can lead to distorted structures, too strong or weak interactions with water and ions, too high or low affinity to the surface, etc. Thus, one has to take care while parameterizing new residues. In the case of nucleobases (Chapter 1.2.2) standard RESP procedure [Cornell, 1993] to get partial charges was sufficient since these molecules are quite standard and represent subunits of the well-parameterized nucleotides. In the case of oxalic acid and its anions, situation was more complicated and required more complex approach.

3.1.1 Simulation setup

Periodic boundary conditions AIMD simulations based on Born-Oppenheimer approximation were carried on using a hybrid Gaussian plane-wave method (GPW) implemented in CP2K software. Charge density cut-off of 400 Ry with NN50 smoothing was used in all simulations. BLYP functional with the empirical dispersion term for the main group elements was used in conjunction with double-ξ molecularly optimized basis functions augmented by polarization function (DZVP) and appropriate pseudopotential of Goedecker, Teter and Hutter (GTH). All hydrogens were replaced by deuterium to reduce quantum effects of the hydrogen nuclei and to increase the time step. Each simulation box
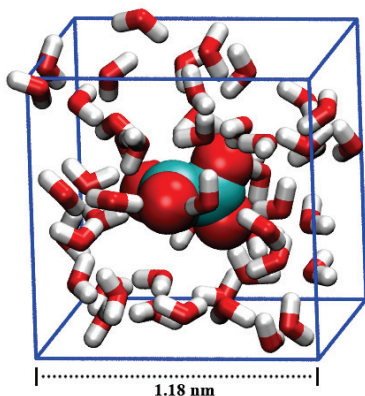
Figure 3-1. AIMD simulation setup. Oxalate dianion by vdw spheres and water by licorice representation.

(Figure 3-1) was composed of (hydrogen) oxalate anion and 50 heavy water (D_2O) molecules. The net charge of the system was compensated by the neutralizing background charge. Production runs were carried out within NVT ensemble with a Nosé-Hoover thermostat and time step of 1 fs. A temperature was set to 300 K and each trajectory was 30 ps long.

Classical MD simulation in NVT ensemble had been performed during parametrization phase with one oxalate ion and 918 water molecules. The net charge of the system was compensated by the neutralizing background charge. Simulation step was set to 1 fs, temperature to 300 K and trajectories had been 2.5 ns long. *Gaff* force field with partial charges derived by standard RESP procedure had been used both for oxalate and SPC/E model of water.

3.1.2 Results

First, we have focused on both forms of oxalic acid anions, i.e. hydrogenoxalate anion and oxalate dianion, in computational study that has combined ab initio optimizations with ab initio molecular dynamics [OK4]. We have confirmed that the most stable conformation of oxalate dianion both in gas phase and in the implicit solvent is the staggered D_{2d} form. From AIMD calculations we have seen that the rotational barrier around C-C bond can be relatively easily overestimated in the explicit solvent. Preferred conformation remains the staggered one in explicit solvent, but it can partially deviate (~20°) from the ideal value. Regarding hydrogenoxalate anion, we have found discrepancy between implicit and explicit solvent calculations: while implicit solvent (and gas phase) calculations predicted global minimum to be the planar structure (*ox-1-closed* in Figure 1-1), where hydrogen of COOH group is involved in intramolecular hydrogen bond with neighboring COO$^-$ group, the AIMD calculations predicted staggered conformation in the presence of more than 8 water molecules and in the bulk. The rotation around C-C bond was almost free at the room temperature in the bulk. It was shown that the solvation pattern around negatively charged carboxylate group is very similar for both anions with approximately 2.5 water molecules around each oxygen, and number of water
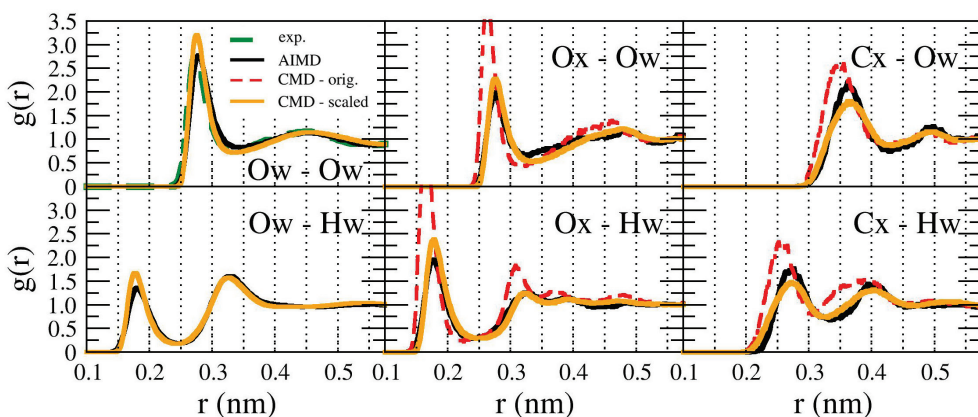
Figure 3-2. Radial distribution functions between water oxygen (top)/hydrogen (bottom) and oxalate dianion oxygen and carbon. Comparison between AIMD data (black), CMD fit with full charges (red, dashed) and scaled charges (orange). Ox stands for oxalate oxygen and Cx for oxalate carbon, respectively.

molecules in the first solvation shell (~15) was found to be the same for both anions and in the agreement with previously reported data [Rosas-García, 2013; Gao and Liu, 2005].

With AIMD data serving as a benchmark, we have designed new model of an oxalate
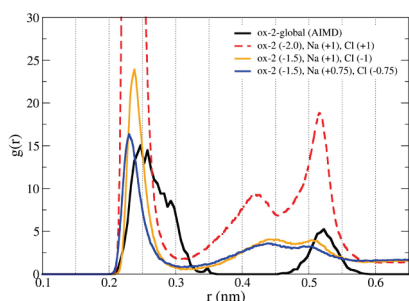

Figure 3-3. Radial distribution functions between oxalate oxygen and sodium cation. 10 ps long AIMD run (black) is compared to CMD simulations with full charges on all ions (red, dashed), scaled charges on oxalate (orange) and scaled charges on all ions (blue).

dianion. Standard RESP procedure combined with Antechamber routine was applied to get partial charges and all bonding and nonbonding parameters. However, resulting model showed exceptionally strong interactions with water (Figure 3-2) and ions (Figure 3-3), as indicated by red dashed curves in both graphs. Especially overshooting of interaction with sodium ion could lead to unrealistic adsorption behavior. This is probably caused by relatively large charge localized on two functional groups close to each other. Thus, we have adopted the concept of MDEC (Molecular Dynamics in Electronic Continuum), alternatively

also called ECC (electronic continuum correction), [Leontyev and Stuchebrukhov, 2012] and according to this concept we have scaled down all partial charges on an oxalate dianion to give 75% charge of the ion, in this case -1.5e. Resulting rdf's between oxalate oxygen/carbon and water oxygen/hydrogen are in good agreement with AIMD data (Figure 3-2). Similarly, interaction with sodium ion has improved considerably (Figure 3-3). In our final choice, charge on sodium ion is scaled down to +0.75e and agreement between CMD and AIMD is even better.

3.2   Physisorption of nucleic acid building blocks

We have focused on studying interactions of nucleobases with quartz (101) surfaces of various charge to bring molecular modeling much closer to real conditions. The main goal is to provide a detailed description of the binding behavior of the four nucleobases (guanine, cytosine, adenine, thymine) to see the influence of the surface charge, to show the best binding arrangement, and to quantify the strength of their interactions with the inorganic surface. Simulated quartz surfaces cover the surface charge densities 0.00, -0.03 and -0.06 $C.m^{-2}$, approximately corresponding to pH values 4.5, 8.5 and 9.5.

3.2.1   Simulation setup

For simulations of a nucleobase adsorption, we prepared box with dimensions $5.50 \times 3.98 \times 24.00$ nm (Figure 3-4) and two quartz (101) slabs with equally charged (or neutral) surfaces positioned in the middle of the box. The gap between slabs (~5.3 nm) was filled with 1 nucleobase (~ 0.01 M), sodium and chloride ions (giving conc. 0.13 M) and approx. 5400 water molecules. Modified ClayFF force field for quartz [OK1] was used in combination with SPC/E water model. Amber99SB force field for nucleobases was completed by partial charges generated by RESP procedure.
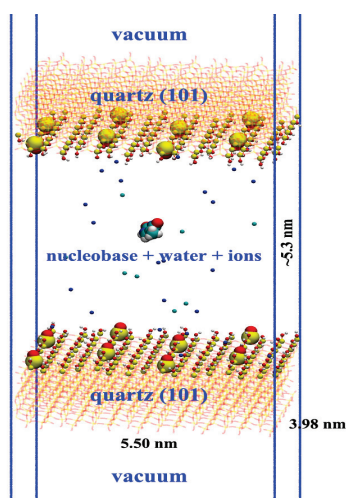

Figure 3-4. Simulation setup. Silanol groups shown by a ball-and-stick and deprotonated silanols by vdw spheres.

Simulation protocol consisted of and equilibration phase in NVT (200 ps) and NPT ensemble (200 ps), followed by production run in NVT ensemble for 100 ns. Time step was set to 2 fs and temperature to 298 K. Other setting were similar to those in [OK1].

3.2.2 Results

During 100 ns runs nucleobases have undergone several adsorption/desorption events on both quartz surfaces in the simulation cell. We have plotted z coordinate of the center of mass of the nucleobases and using these plots we have determined borders limiting adsorption event. Structures within these limits were analyzed.

Bivariate plots can unambiguously describe orientation of the nucleobase above the surface [Jedlovszky, 2006]. Bivariate plot is a combined plot of two angles, one between vector p and z axis and second between vector o and z axis. Both vectors are depicted in Figure 1-2. Adenine is the only nucleobase without oxygen in the structure and shows the most distinctive adsorption motifs among studied nucleobases (Figure 3-5). For neutral surface, there is one characteristic adsorption structure around angles (75, 20) indicating binding motif with N7 atom and NH_2 group making hydrogen bonds with silanol group.
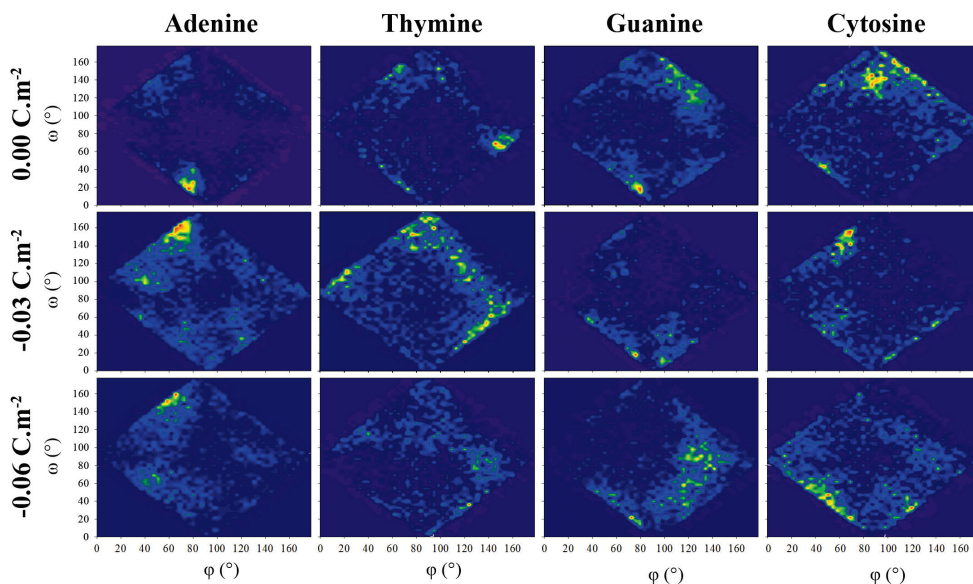

Figure 3-5. Bivariate plots showing orientation of the adsorbed nucleobases. φ is an angle between vector p and z axis and ω is an angle between vector o and z axis. For definition of the vectors see Figure 1-2.

On surfaces with charge densities -0.03 and -0.06 C.m^{-2}, adenine behaves similarly being adsorbed by N9H group (70, 160). Thymine is remarkable due to its bulky hydrophobic CH$_3$ group. Thymine interacts by N1H group and O2 with uncharged surface (160, 80) with second maximum around (70, 150), i.e. interaction by N1H group. On -0.03 C.m^{-2} surface, thymine shows wide scale of adsorption motifs, going from O4 through N3H and O2 to N1H group. Adsorption motif of thymine on -0.06 C.m^{-2} surface is hardly recognizable. Guanine on neutral surface binds mainly by its nitrogen groups N9H, N3 and NH$_2$ (120-140, 120-140), accompanied by portion of structures adsorbing by O6 atom (80, 20). The same structure occurs on charged surface, in the case of the -0.06 C.m^{-2} surface completed by structures interacting by NH$_2$ and N1H (120-140, 20-90). Cytosine interacts mainly by O2, N3 and NH$_2$ group on uncharged surface having slightly tilted position (90, 140). On -0.03 C.m^{-2} surface the predominant adsorption site is (60, 140) NH$_2$ group with N3 nitrogen. Contrary, on -0.06 C.m^{-2} surface cytosine interacts the most by its hydrophobic part, i.e. two CH groups (35-70, 30-60).

These preliminary results suggest that each nucleobase behaves uniquely and it is hard to find any unifying binding motif even within purine or pyrimidine bases. The only binding motif occurring in multiple systems is the one where one nitrogen (or oxygen) of nucleobase forms hydrogen bond with hydrogen on one silanol group, and simultaneously NH or NH$_2$ group binds to oxygen on another silanol. Work on other results, including role of ions or deprotonated silanol groups, is in progress.

3.3   Physisorption of an oxalate dianion

Hydroxylated rutile (110) surface with new parameters by Brandt and Lyubartsev (Chapter 2.4) together with oxalate dianion with newly developed parameters (Chapter 3.1) were combined to simulate adsorption of this chemical compound.

We have focused on uncharged and positively charged surfaces, since these particular surfaces are the most attractive for oxalate dianions, as observed experimentally by Ridley *et al.* [pers. comm., 2016].

Figure 3-6a shows plot of the axial density of the oxygen is oxalate above hydroxylated rutile surface with surface charge densities 0.00 and +0.10 C.m^{-2}. For comparison, corresponding water oxygen density profiles are included. One can notice that Ox of oxalate can interact with surface very similarly as Ow of water – the position of the first peak (~0.37 nm) is very similar. Regarding the 2nd peak around 0.6 nm, the story can be much more complex for oxalate. First possibility is that this peak represents outer
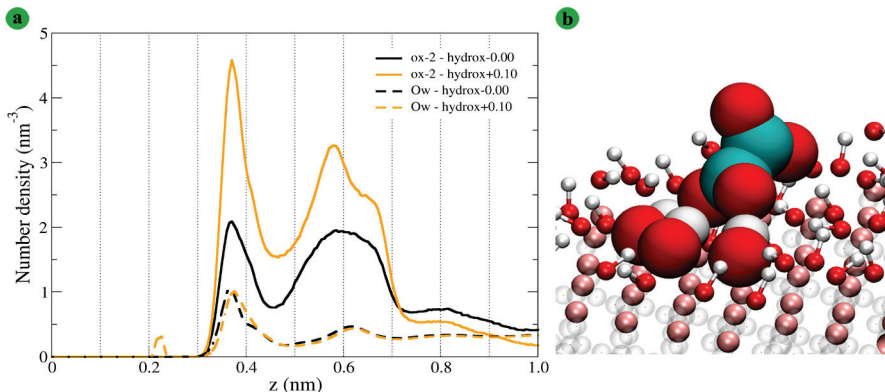
Figure 3-6. (a) Axial density profile of the oxalate dianion on hydroxylated rutile surface with surface charge density 0.00 $C.m^{-2}$ and +0.10 $C.m^{-2}$, y axis values of the water oxygen profiles are scaled down by 100; (b) Snapshot of the typical adsorption motif.

sphere oxalate, i.e. oxygen of oxalate which does not interact directly by any of its (four) oxygens with surface atoms. Alternatively it can represent another oxalate oxygen of oxalate molecule interacting directly with the surface via another oxygen atom. Not surprisingly, oxalate axial density near the surface increases with increasing positive surface charge due to enhanced electrostatic attraction. Figure 3-6b shows snapshot of a typical adsorption configuration.

Further work on this topic is the current focus of the work of doctoral student Denys Biriukov and is beyond the scope of this thesis.

4. Chemisorbed biomolecules

4.1 Chemisorbed nucleic acid on a graphene surface

From the chemical point of view, work on the chemisorbed nucleic acids on graphene surface [OK2], follows and extends work on physisorption of the nucleic acid bases on a quartz surface. This study is tightly connected to biosensing, microarrays or DNA chips, and its main purpose was to investigate the role of the surface charge density in the structure and orientation of covalently attached single-stranded and double-stranded DNAs (Chapter 1.2.3).

The graphene surface (Chapter 2.2) has been selected as the substrate in our simulations, because it is a relatively simple but realistic surface and its structure is independent of pH, salt concentration, etc. Finally, some theoretical studies on DNA interaction with carbon nanotubes (i.e. with surfaces based on graphene geometry) have already been conducted [Hummer, 2001; Lu, 2005; Zhao, 2007; Johnson, 2009]. The binding of DNA to carbon nanotubes has been identified as a way to open the door to carbon-nanotube-based applications in biotechnology [Zheng, 2003].

4.1.1 Simulation setup

Full simulation setup was described in detail in [OK2]. Just few parameters important for comparison with peptide/mercury system (Chapter 4.2) are mentioned here.

Simulation box is depicted on Figure 4-1. Two graphene layers of size of 6.81×6.64 nm and separation 6.33 nm enclose space for water, ions, and DNA attached to a charged surface. The role of the second graphene surface, which was always neutral, was to close the system. In order to minimize the influence of the electric field generated by the
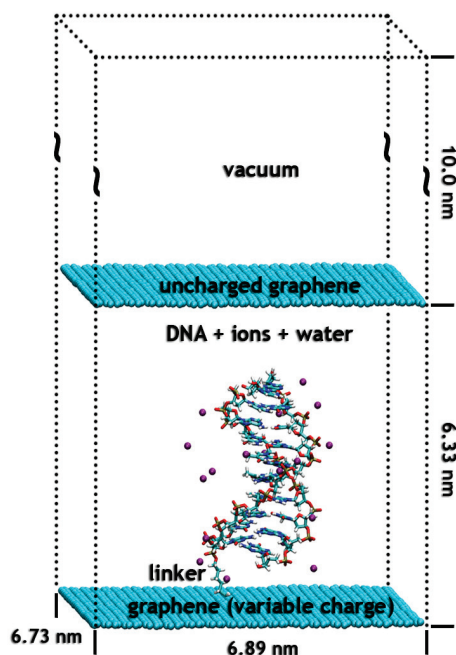
Figure 4-1. A schematic representation of the simulated system.

charged graphene layer on the periodic images, the replicas of the system were separated by a 10 nm vacuum gap. Similar setup was used later for peptide/mercury system (Chapter 4.2).

ds-DNA and ss-DNA decamers with the base sequence 5'-CCACTAGTGG-3' at the canonical B-form were covalently bonded to the graphene layer via an aliphatic carbon linker consisting of six methylene groups (C6). The linker was attached to the 5' end of the cytosine nucleotide by the phosphodiester bond. In the initial position, the DNA helix axis was orientated perpendicularly to the graphene slab.

In order to test the role of the charge of the graphene layer on the position and the orientation of the DNA, all of the carbon atoms of the graphene layer, to which DNA is anchored, were charged to one of the following values: -0.1, -0.05, -0.02, -0.01, 0, +0.01, +0.02, +0.05 or +0.1 elementary charge (e) per carbon, corresponding to the range of the surface charge densities -0.594 to +0.594 $C.m^{-2}$ (see Table 2-3) comparable to those used in the experiment. The sodium/chloride ions were used in order to neutralize fully the charge applied on the graphene, whereas the DNA was neutralized independently by sodium cations.

All of the molecular dynamics simulations were carried out with an atomic resolution including all the hydrogens and in explicit water. An equilibration protocol consisted of a series of energy minimizations and short restrained NPT MD runs. The equilibration phase was followed by an NVT MD production run at 298 K. The restraint of 10 $kcal.mol^{-1}.\mathring{A}^{-2}$ on all of the graphene atoms was used for the production run in order to keep the graphene layer planar during the simulations. The separation of the two graphene layers in the *z*-direction, 6.33 nm, was sufficient to prevent the interaction of the 3'-DNA terminus with the neutral graphene layer. Each trajectory covered 50 ns.

4.1.2 Results

The probe surface excess concentration used in our study $\Gamma_P = 3.32 \times 10^{-12}$ mol.cm^{-2} was selected to be of the same order of magnitude as a microarray maximum sensitivity for a 10-mer long probe ($\Gamma_P = 9.96 \times 10^{-12}$ mol.cm^{-2}) [Vainrub and Pettitt, 2003]. Probe surface excess concentration used in peptide/mercury study (Chapter 4.2) was comparable, $\Gamma_P = 2.68 \times 10^{-12}$ mol.cm^{-2}.

For comparison with peptide/mercury system just results for ss-DNA are highlighted here. Detailed results can be found in the original manuscript [OK2].

The ss-DNA exhibits ordered stacked helical structure if left free in solution, but it shows localized structural collapse when a graphene layer is present, even if it is not charged. In neutral system, interactions between the surface and the ss-DNA confirm both the experimental and theoretical results, that more bases than merely the first one are adsorbed to the surface because of the higher flexibility of the ss-DNA.

For low negative charge density (-0.01e), an attractive dispersion interaction between the closest base and the graphene layer (majority of the simulation) and attraction of the polar amino group of the closest cytosine and the graphene (shorter periods of the simulation) was seen. For the medium negative charge densities, -0.02 to -0.05e, the electrostatic interactions become the leading factor for the stabilization of the DNA-graphene complex and the attraction of the amino group of the closest cytosine and the surface is crucial. In addition to these interactions, in the -0.05e system, the interaction of the negatively charged sugar-phosphate backbone in the middle part of the ss-DNA with the counterions localized close to the surface is observed as well. In systems with the highest applied negative charge density on the graphene (-0.1e), an oppositely charged layer of counterions was formed and a strong attraction of the phosphates with the sodium cations was observed immediately after the beginning of the simulation.

In the system with lowest positive surface charge (+0.01e), approximately after 10 ns of the simulation the whole ss-DNA is localized close to the surface and interacts via phosphates (by electrostatic forces) and as well as with majority of its bases (by dispersion forces) with the surface. When the charge of the carbons in graphene is changed to +0.02e, the electrostatic attraction between the phosphates and the surface causes a parallel orientation of the DNA already in the early stage of the simulation. In addition, an electrostatic interaction of the guanine with the surface mediated via the O6 oxygen atom of the base is observed. Occasionally, one or few bases still interact with the surface by dispersion forces. For the system containing graphene with a charge of +0.05e on the carbon atoms, the electrostatic forces attracting the phosphates to the surface are crucial,

but it takes about 10 ns before the parallel orientation of the DNA with the surface is reached (probably owing to the presence of a non-negligible amount of chloride anions next to the surface). At the surface with a charge of +0.1e, the ss-DNA remains extended and perpendicularly orientated to the graphene surface covered by an almost immobile layer of counterions (Cl⁻) at the beginning of the simulation. This rather strong repulsion between the chloride anions and phosphates leads to the extension of the linker as well as the DNA.

4.2 Chemisorbed peptides on a mercury surface

Having experience with simulations of graphene surface and chemisorbed oligonucleotides, we have joined experimentalists J. Vacek (Department of Medical Chemistry and Biochemistry, Palacký University Olomouc) and V. Dorčák (Institute of Biophysics, Brno) who have studied peptides on mercury electrode by label-free electrochemical method called constant-current chronopotentiometric stripping (CPS, Chapter 1.2.4). Method was described in detail in experimental and theoretical study by Dorčák *et al.* [OK3]. In this study, proton transfer ability of peptidic H-wires was characterized experimentally in an adsorbed state using an approach based on a label-free electrocatalytic reaction. The experimental findings were complemented by theoretical calculations on the ab initio level in vacuum and implicit solvent. Experimental and
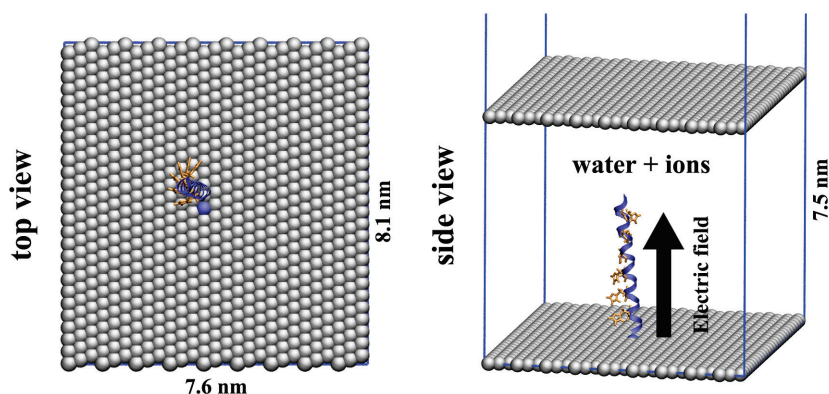

Figure 4-2. Initial configurations of studied systems. Top and side view of the simulation box. Histidine residues are highlighted by orange color and licorice representation, anchoring surface mercury atom is highlighted by blue color.

theoretical results indicated $Ala_3(His-Ala_2)_6$ to be a high proton-affinity peptidic H-wire model.

As a follow-up to experimental and ab initio results, we continued with MD simulations. Our task was to prepare and simulate systems with different surface charge densities, with different densities of the chemisorbed peptides and with different protonation state of the histidine residues to show how these three parameters influence conformations and dynamics of the peptide strands covalently attached to mercury surface. Our findings should support experimental data [OK3] and give detailed insight on the molecular level.

4.2.1 Simulation setup

Verification of the proper parameters for the mercury surface was described earlier in Chapter 2.2.

The simulated system is depicted in Figure 4-2. All the simulations were carried out in a periodic box with dimensions 7.6 × 8.1 x 100.0 nm. Water, ions and peptide were confined between two solid monolayer mercury surfaces; one surface was positioned at $z = 0$ and the second one in $z = 7.5$ nm. Similarly to previous study with graphene surface, role of the upper surface was to close the system. Overall height of the simulation box was set to 100 nm to suppress influence of the applied electric field on images of basic simulation box in z direction. A 21-mer peptide of sequence AAA HAA HAA HAA HAA HAA HAA peptide (Figure 4-3a) was covalently anchored to the mercury surface through modified cystein residue. Two possible protonation states of histidine residues were systematically employed in our simulations (Figure 4-3b): a) all histidines were neutral with proton on ε-nitrogen atom of the imidazole ring (system abbreviated as "HIE" in the following
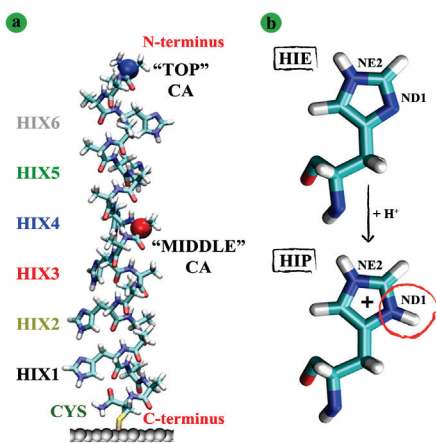

Figure 4-3. a) Top CA carbon atom (blue) and middle CA carbon atom (red) used for further analysis highlighted by vdw sheres representation. Color coding of the histidine residues used in following graphs shown on the left; b) Neutral (HIE) and protonated (HIP) histidine residues.

text); b) all histidines were protonated with protons both on ε- and δ-nitrogen atoms of the imidazole ring (system abbreviated as "HIP" in the following text).

The ionic strength of the NaCl solution was set to 0.05 M to mimic usual experimental conditions. The charge on mercury surface was realized by application of the voltage between the mercury surface and opposite wall of the periodic box. The series of voltages -50 V, -25 V, -10 V, -1 V, 0 V , +1 V, +10 V, +25 V, +50 V was applied in the simulations with one peptide strand (for corresponding surface charge densities see Table 2-3). Voltage between two mercury surfaces was generated by setting up the appropriate electric field times the height of the gap between these surfaces (7.5 nm). During 2 ns long equilibration phase only water molecules and ions were allowed to move, while peptide was held in its upright position applying position constraints. Simulation time of the production run was 50 ns for each trajectory. During production run all the molecules except mercury surfaces were allowed to move.

4.2.2   Results

System with only one peptide strand represents limiting situation where interactions with neighbor strands are excluded and the anchored peptide is moving freely under given conditions. Surface excess concentration for this setup is $\Gamma_P = 2.68 \times 10^{-12}$ mol.cm^{-2}, corresponding to the available area for one peptide strand $a_P = 62.06$ nm^2.

HIE system. Time evolution of positions of middle and top points on peptide backbone is depicted in Figure 4-4. The initial conformation oriented perpendicularly to the surface has a tendency to slowly approach the surface and adsorb on it. The center of the peptide started interacting with the surface no later than in 20 ns under any applied electric field. Even the top of the protein in negative and low positive voltages can be found in the vicinity of the surface. Only the highest applied positive voltages (+25 V and +50 V) cause notable fluctuations of this part of the peptide. This can be caused by repulsion between surface and positively charged N-terminus of the peptide. Despite these fluctuations, results clearly indicate an effort of the peptide to maximize the interaction with the surface, no matter what value of the voltage is applied. This view is supported by Figure 4-5a where time evolutions of distances of the imidazole rings from the surface are depicted. Positions of side chains fluctuate notably only when voltage of +50 V is applied, otherwise all the imidazole rings are located no farther than 1 nm from the surface during analyzed time.

HIP system. As one can expect, the electrostatic forces between charged histidines (HIP) and mercury surface influence behavior of the peptide-surface complex.

On the first sight and rather surprisingly, there are not so big differences between orientation of protonated and deprotonated peptide relative to the mercury layer. The time evolutions of their distances from the surface are similar both for HIE and HIP systems for majority of applied voltages (Figure 4-4). Only when highly positive voltages of +25 V and +50 V were used, HIP system shows enhanced fluctuations of its middle part compared to the HIE system with neutral histidines since parts of the peptide are more repealed from the surface forming various kinks and loops. Although the upper end of the peptide is adsorbed on the surface, the central part remains desorbed, making loop with positive histidine residues pointing out of the surface. On the other side, this also illustrates that relatively high positive charge on the surface cannot fully prevent positively charged residues from approaching the vicinity of the surface. Stacking interactions between the surface and the histidine residues as well as the hydrophobic
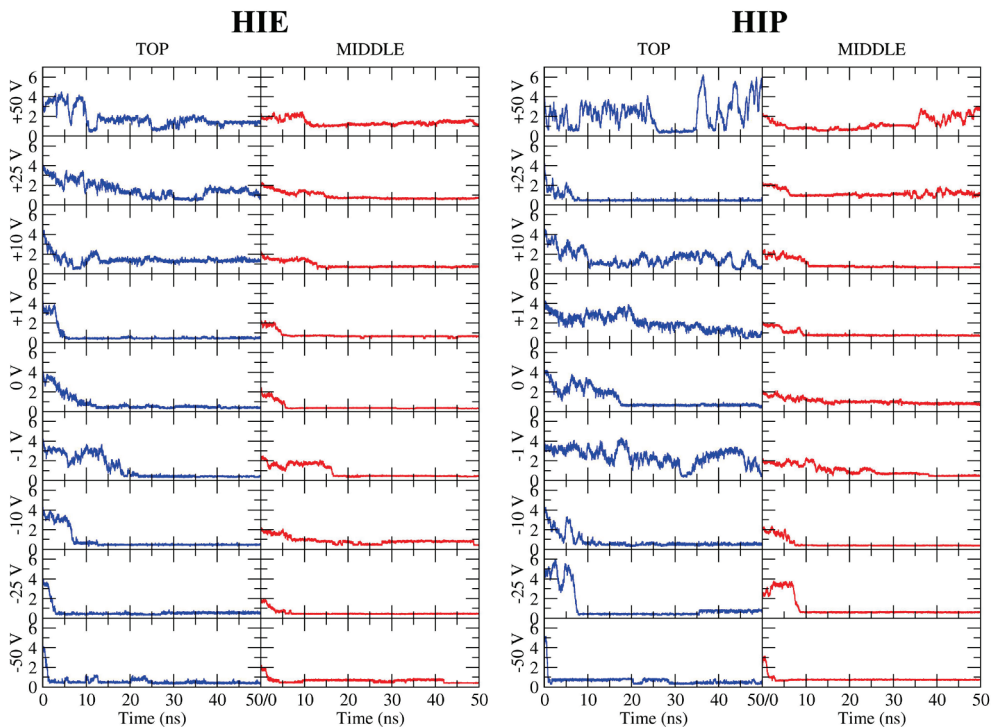

Figure 4-4. Time evolution of the *z* coordinates of the two points on protein backbone for 1 strand system. "TOP" is the CA carbon on the alanine most distant from the surface at the initial configuration; "MIDDLE" refers to CA carbon on middle alanine (see Figure 4-3a). Results in the left column are for deprotonated histidine (HIE), results in the right column for protonated histidine (HIP).
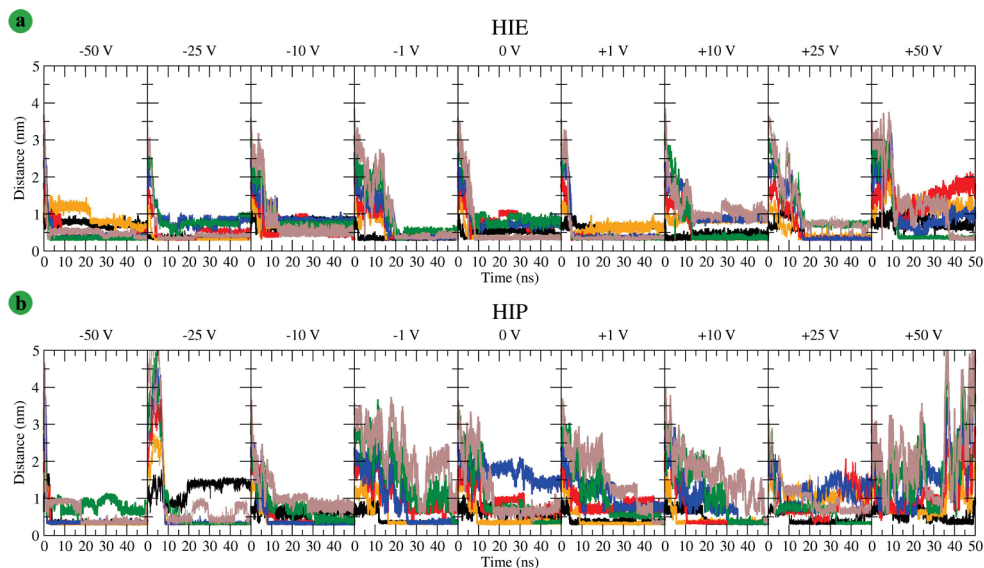
Figure 4-5. Time evolution of the z coordinates of the geometric centers of the heavy atoms in imidazole rings. Color coding according to Figure 4-3. (a) for HIE system and (b) for HIP system.

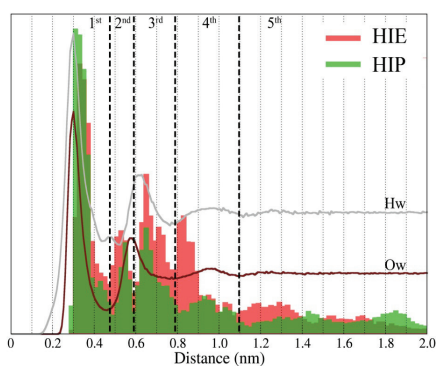interactions of the alanine residues (CH_3 group) can stand behind this behavior.

Figure 4-6. Merged histograms of the z coordinates of the geometric centers of the heavy atoms in imidazole rings for all applied electric fields. Axial density profiles of water oxygen and hydrogen included.

Graph with time evolution of the z coordinates of the geometric centers of the imidazole rings (Figure 4-5b) shows that in the most negative system all imidazole rings except one are located within 0.3 nm from the surface. In -25 V system electrostatics still pushes histidine residues close to the surface and number of the adsorbed species is greater than in the HIE system. While in -10 V system charged histidine residues behaves similarly as in the matching HIE system, starting from -1 V system histidine residues show greater fluctuations and, thus, positions close to the surface are less populated at the expense of the peaks far from the surface. Difference between neutral and charged

histidine residues is most visible for +25 V and +50 V systems, where fluctuations in the HIP systems are considerable.

Position of imidazole rings. If we merge histograms of perpendicular positions of the imidazole rings for all applied voltages in HIE and HIP systems, four well separated peaks appear (Figure 4-6). The same holds true even for HIP system. Peaks are approximately located at regions 0 - 0.47, 0.48 - 0.57, 0.58 - 0.78 and 0.79 - 1.02 nm above the surface. A probable reason for this discrete arrangement of histidine residues is an inability of adsorption of all histidine residues to the surface due to steric reasons and structured water near the surface. Water oxygen density profile is depicted in the same graph as merged histograms (Figure 4-6). One can see that up to ~1 nm imidazole rings are mostly positioned between minima and maxima of the water oxygen density curve. This curve shows two distinct peaks positioned at 0.3 and 0.58 nm, respectively. In the case of HIE system the more distant peaks are more populated due to overall lower affinity of this system to the surface than in HIP system.

4.3   Discussion

There are certain similarities in both studies that dealt with chemisorbed biomolecules. First, in both studies an atomically flat surface with a regular structure was used as a substrate. Second, positive and negative electric fields were applied in both systems and to some extend their intensities overlapped (see Table 2-3). Third, DNAs and peptides with protonated histidines (HIP system) carry significant charge, although one has to keep in mind that these charges have opposite values and are located on different parts of biomolecules (ss-DNA backbone vs. histidine residue). And finally, both used biomolecules contain heteroatomic aromatic rings that can be involved in similar type of the weak intermolecular interactions.

In the following text we will focus on ss-DNA/graphene systems denoted as 0.00, ±0.01 and in the original manuscript [OK2] and on peptide/mercury systems denoted as 0 V and ±50 V in previous chapter, because according to the Table 2-3 these systems have comparable voltage applied in a simulation cell. But it is important to recall different approach to generate electric field in a simulation cell. While in ss-DNA/graphene simulations electric field was generated by partial charges on each carbon atom in a substrate, in peptide/mercury simulations external electric field was applied by switching on corresponding option in Gromacs software. An approach applied in ss-DNA/graphene

simulations required enormous number of the compensating ions in the simulation cell and this could lead (besides other factors) to differences in two studied systems.

Comparing systems with no voltage applied (Figure 4-7, middle graphs) is the most straightforward. One can see that it took ss-DNA molecule almost 40 ns to get close to the surface, while HIP peptide reached the surface in 20 ns. In neutral HIE peptide, middle part of the peptide reached surface even faster, within less than 10 ns. But overall behavior is very similar. Short initial period where ss-DNA/peptide strand remained in upright position was followed by sorption of other nucleobases/imidazole rings and this led after several nanoseconds to a spreading of the strand onto the surface with some nucleobases/imidazole rings stacked and some not. Figure 4-8 illustrates this on snapshots with typical conformations. For ss-DNA this behavior on graphene surface was supported by other experimental and theoretical studies [Hummer, 2001; Zhao, 2007; Johnson, 2009]. In the case of peptide, it is hard to find supporting data due to unusual substrate and specific peptide constitution. It was suggested for pH neutral solution of the histidine amino acids, that the orientation of neutral HIE or charged HIP on the mercury electrode [Słojkowska and Jurkiewicz-Herbich, 1999] was with the neutral imidazole ring perpendicular to the Hg surface and NH_3 group also directed towards the metal. Contrary, study conducted on gold surface concluded, that the HIE molecules are adsorbed through
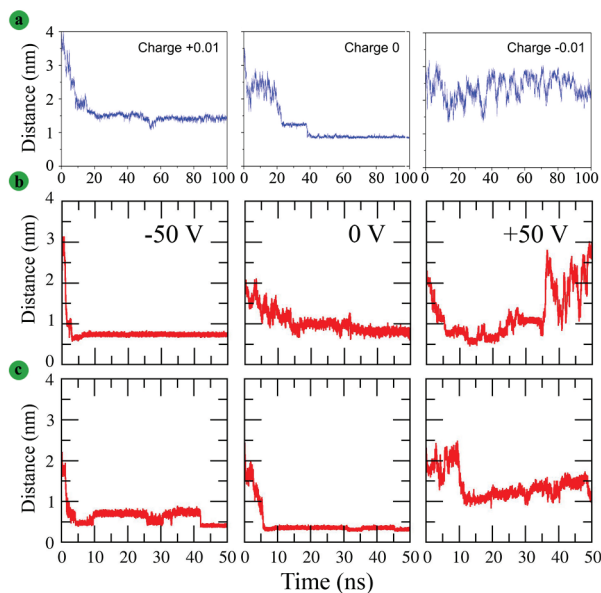

Figure 4-7. The distance of the (a) central phosphorus atom (in nm) of ss-DNA; and (b) middle CA atom of the HIP peptide strand; and (c) middle CA atom of the HIE peptide strand to the graphene and mercury layer, respectively.

the deprotonated nitrogen atom of the imidazole ring and with NH_3 group located nearer to electrode than COO^- [Lim, 2008]. One has to keep in mind, that these studies dealt just with amino acids in solution. Theoretical study on adsorption of the amino acids on the gold substrate [Hoefling, 2010] predicted very high affinity of amino acids with aromatic rings to the gold. Another study [Iori, 2009] also found stronger-than-expected interactions for aromatic amino acids. It was suggested [Hoefling, 2010] that these strong interactions may be caused by π-electron mediated effects and, simultaneously, the planarity of aromatic amino acids allows maximizing the dispersion interaction with the equally planar surface.

Positive voltage in ss-DNA/graphene system has the same effect as negative one in peptide/mercury system (Figure 4-7 and Figure 4-8, left graphs). In +0.01 ss-DNA system,
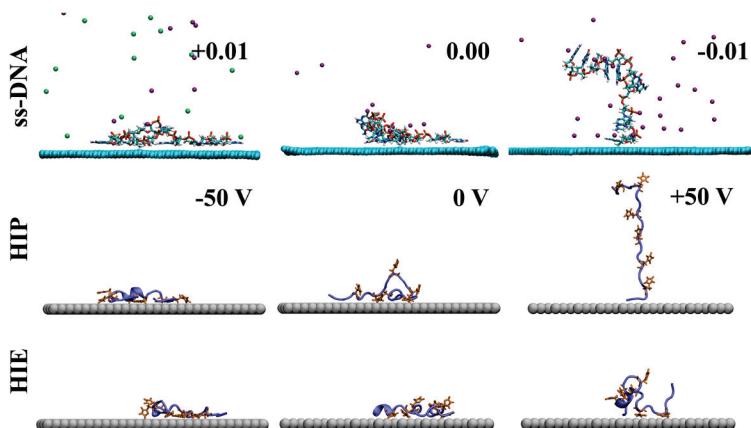

Figure 4-8. The typical conformations of ss-DNA, HIP and HIE peptides after the equilibrium is reached.

ss-DNA benefits from the mutual cooperative effect of the electrostatic and dispersion interactions and after few nanoseconds the whole ss-DNA is localized close to the surface and interacts via phosphates (by electrostatic forces) and as well as with majority of its bases (by dispersion forces) with the surface (80 %, Figure 4-9). In -50 V HIP system, the strands collapse on a shorter time scale (<5 ns) compared to +0.01 ss-DNA, but the number of the adsorbed heterocycles is similarly 80 % (Figure 4-9) and peptide adopts flat conformation as ss-DNA. Lower attraction between HIE system and negative surface compared to HIP system causes lower number of the stacked imidazole rings and structure with several kings.
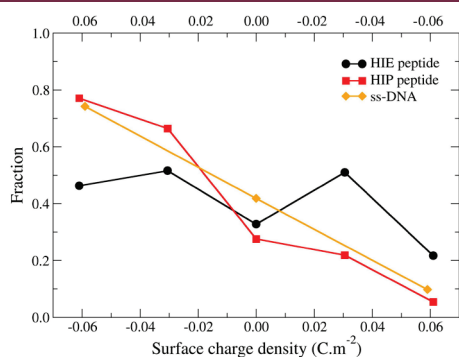
Figure 4-9. Fraction of the adsorbed nucleobases and imidazole rings in ss-DNA/graphene and peptide/mercury systems, respectively. Heterocycles were considered as stacked when N1/NE and N3/ND atoms in their heteroatomic rings were within 0.45 nm from the surface. Upper horizontal scale is for ss-DNA/graphene.

Negative voltage in ss-DNA/graphene system and positive one in peptide/mercury system causes notable fluctuations of the strands (Figure 4-7 and Figure 4-8, right graphs). Electrostatic repulsion plays key role here while stacking interactions are suppressed, especially in the ss-DNA/graphene system. Mutual repulsion of the sugar-phosphate backbone and surface leads to bent structure of the ss-DNA with just first nucleobase stacked onto the surface (Figure 4-9). Peptide systems with negative voltage are highly dependent on protonation state of the histidine residue. Whereas HIE system shows mild response on increasing voltage and structures are still very close to the surface, remarkable fluctuations and upright position can be seen for the highest voltage applied in the HIP system (Figure 4-8). Similarly to negative surface charge, number of the stacked imidazole rings in HIP system is comparable to number of stacked bases in ss-DNA system.

5. Conclusion

This thesis represents author's effort to learn advanced computer modeling methods and to apply them to study interactions of biomolecules with mineral surfaces. Where necessary, auxiliary studies (in terms of the main goal of this thesis, but otherwise representing interesting studies themselves) of interactions of molecules with the aqueous solutions without a presence of surfaces or interactions of water and ions with the surfaces (inevitable to understanding of the adsorption of molecules) were carried out. As a result of this effort three articles on adsorption and two others that dealt with biomolecules in water were published in international peer-reviewed journals. One more is submitted.

Four different surface models were prepared, parameterized and used in simulations. Special effort was paid to the quartz (101) surface that was parameterized to reflect its nature under neutral and basic pH conditions [OK1], i.e. to device models of charged surface corresponding to these conditions. The validity of the quartz and graphene surface [OK2] models was confirmed by comparison with experimental data. In both case, agreement in positions of the structured water molecules above the surface was satisfactory. Fairly good agreement was found in positions of the rubidium ions above the quartz surface, where two experimentally observed peaks were suggested to be completed with one more peak positioned between these two. In the case of the mercury surface, several parameters taken from literature were compared with ab initio derived data. The best matching parameters were used in subsequent study on chemisorption of peptides. Due to compatibility issues, well-established parameters by Matsui and Akaogi for rutile surface were replaced by parameters by Brandt and Lyubartsev that suit better for systems combining inorganic surface with biomolecules. Since good agreement was found, rutile surfaces with implemented Brandt and Lyubartsev parameters were used in subsequent oxalate adsorption study. All prepared models will serve for further simulations in the Předota's group.

Prior to an adsorption study, oxalate dianion and hydrogenoxalate ion were inspected by means of AIMD to get detailed information about structures and solvation shells of these species [OK4]. Oxalate was confirmed to adopt staggered conformation in water. The most stable conformation of a hydrogenoxalate from ab initio optimizations in implicit solvent was denied by AIMD in explicit water environment. Extended analysis supported AIMD results that predicted disruption of intramolecular hydrogen bond and transitions from planar to staggered structure is correct. Solvation shell of both ions was described in detailed and final results served as benchmark for oxalate model parameterization. RESP procedure was used to derive first trial model of an oxalate for CMD. Subsequent tuning of partial charges together with bonded and non-bonded parameters led to new model of oxalate dianion that should behave properly in contact with water and ions.

Preliminary results for physisorption of the oxalate on a rutile surface and nucleobases on a quartz surface were presented here. Different adsorption patterns of four nucleobases were revealed with a help of bivariate plots. Results suggested that each nucleobase behaves uniquely and it is hard to find any unifying binding motif even within purine or pyrimidine bases. Regarding oxalate on rutile surface, it was shown that despite its high negative charge oxalate occupies similar positions as structured water above the surface. An adsorption activity increased with increasing positive charge on a surface. Further work on this topic is currently followed by another doctoral student .

Two published studies dealt with chemisorbed biomolecules: in one of them we studied single- and double-stranded DNA on a graphene surface [OK2] and in other we focused on peptide wires on a mercury surface [OK3]. Study of DNA on a graphene surface outlined the role of surface charge on DNA adsorption and found notable differences in ss- and ds-DNA adsorption. While in ds-DNA electrostatic forces between charged surface and ds-DNA backbone play major role, in ss-DNA stacking interactions become also involved and in particular cases stacking interactions can compete with electrostatic forces, making adsorption of ss-DNAs more varied compared to ds-DNA. In combined experimental and ab initio study [OK3], ability of peptides with particular composition to act like proton wires was confirmed. Subsequent CMD study focused on a more detailed analysis of chemisorbed peptide(s). Mainly the role of the surface charge in combination with different protonation states of the histidine residues was described. While peptides with neutral histidines were found to be rather insensitive to different surface charge, peptides with protonated histidines showed greater sensitivity to surface charge applied.

To summarize, in this thesis the author attempted to demonstrate the applicability of methods of molecular dynamics to describe adsorption of various chemical species (going from water and ions through small organic molecules to larger biomolecules) on various types of inorganic surfaces. Since adsorption events stand behind various natural and artificial processes and experimental techniques, presented results provide information relevant for many fields of biophysics.

References

Baú, J., Carneiro, C., de Souza Junior, I., de Souza, C., da Costa, A., di Mauro, E., Zaia, C., Coronas, J., Casado, C., de Santana, H., Zaia, D., 2012. Adsorption of Adenine and Thymine on Zeolites: FT-IR and EPR Spectroscopy and X-Ray Diffractometry and SEM Studies. Orig. Life Evol. Biospheres 42, 19–29. doi:10.1007/s11084-011-9246-1

Bellucci, F., Lee, S.S., Kubicki, J.D., Bandura, A., Zhang, Z., Wesolowski, D.J., Fenter, P., 2015. Rb$^+$ Adsorption at the Quartz(101)–Aqueous Interface: Comparison of Resonant Anomalous X-ray Reflectivity with ab Initio Calculations. J. Phys. Chem. C 119, 4778–4788. doi:10.1021/jp510139t

Berendsen, H.J.C., Grigera, J.R., Straatsma, T.P., 1987. The missing term in effective pair potentials. J. Phys. Chem. 91, 6269–6271. doi:10.1021/j100308a038

Bogdan, D., Morari, C., 2012. Electronic Properties of DNA Nucleosides Adsorbed on a Au(100) Surface. J Phys Chem C 116, 7351–7359. doi:10.1021/jp210229e

Bomont, J.-M., Bretonnet, J.-L., 2006. An effective pair potential for thermodynamics and structural properties of liquid mercury. J. Chem. Phys. 124, 54504.

Bopp, P.., Heinzinger, K., 1998. MD studies of electrolyte solution|liquid mercury interfaces. J. Electroanal. Chem. 450, 165–173. doi:10.1016/S0022-0728(97)00638-4

Bosio, L., Cortes, R., Segaud, C., 1979. Xray diffraction study of liquid mercury over temperature range 173 to 473 K. J. Chem. Phys. 71, 3595–3600. doi:10.1063/1.438817

Brandt, E.G., Lyubartsev, A.P., 2015. Systematic Optimization of a Force Field for Classical Simulations of TiO2–Water Interfaces. J. Phys. Chem. C 119, 18110–18125. doi:10.1021/acs.jpcc.5b02669

Brindley, G.W., Lailach, G.E., Thompson, T.D., 1968. Absorption of pyrimidines, purines, and nucleosides by Li-, Na-, Mg-, and Ca-montmorillonite /clay-organic studies XII/. Clays Clay Miner. 16, 285–293.

Butenuth, A., Moras, G., Schneider, J., Koleini, M., Köppen, S., Meißner, R., Wright, L.B., Walsh, T.R., Ciacchi, L.C., 2012. Ab initio derived force-field parameters for molecular dynamics simulations of deprotonated amorphous-SiO2/water interfaces. Phys. Status Solidi B 249, 292–305. doi:10.1002/pssb.201100786

Butt, H.-J., Graf, K., Kappl, M., 2003. Front Matter, in: Physics and Chemistry of Interfaces. Wiley-VCH Verlag GmbH & Co. KGaA, pp. i–xii.

Carneiro, C.E.A., Berndt, G., de Souza Junior, I.G., de Souza, C.M.D., Paesano, A., Jr, da Costa, A.C.S., di Mauro, E., de Santana, H., Zaia, C.T.B.V., Zaia, D.A.M., 2011. Adsorption of adenine, cytosine, thymine, and uracil on sulfide-modified montmorillonite: FT-IR, Mössbauer and EPR spectroscopy and X-ray diffractometry studies. Orig. Life Evol. Biosphere J. Int. Soc. Study Orig. Life 41, 453–468. doi:10.1007/s11084-011-9244-3

Cleaves, H.J., Jonsson, C.M., Jonsson, C.L., Sverjensky, D.A., Hazen, R.M., 2010. Adsorption of Nucleic Acid Components on Rutile (TiO2) Surfaces. Astrobiology 10, 311–323. doi:10.1089/ast.2009.0397

Cornell, W.D., Cieplak, P., Bayly, C.I., Kollmann, P.A., 1993. Application of RESP charges to calculate conformational energies, hydrogen bond energies, and free energies of solvation. J. Am. Chem. Soc. 115, 9620–9631. doi: 10.1021/ja00074a030

Cygan, R.T., Liang, J.-J., Kalinichev, A.G., 2004. Molecular Models of Hydroxide, Oxyhydroxide, and Clay Phases and the Development of a General Force Field. J. Phys. Chem. B 108, 1255–1266. doi:10.1021/jp0363287

Dimitrov, D.I., Raev, N.D., 2000. Molecular dynamics simulations of the electrical double layer at the 1 M KCl solution | Hg electrode interface. J. Electroanal. Chem. 486, 1–8.

Dorčák, V., Ostatná, V., Paleček, E., 2013. Electrochemical reduction and oxidation signals of angiotensin peptides. Role of individual amino acid residues. Electrochem. Commun. 31, 80–83. doi:10.1016/j.elecom.2013.03.016

Emami, F.S., Puddu, V., Berry, R.J., Varshney, V., Patwardhan, S.V., Perry, C.C., Heinz, H., 2014. Force Field and a Surface Model Database for Silica to Simulate Interfacial Properties in Atomic Resolution. Chem. Mater. 26, 2647–2658. doi:10.1021/cm500365c

Enache, T.A., Oliveira-Brett, A.M., 2013. Peptide methionine sulfoxide reductase A (MsrA): Direct electrochemical oxidation on carbon electrodes. Bioelectrochemistry 89, 11–18. doi:10.1016/j.bioelechem.2012.08.004

Fenter, P., Cheng, L., Rihs, S., Machesky, M., Bedzyk, M.J., Sturchio, N.C., 2000. Electrical Double-Layer Structure at the Rutile–Water Interface as Observed in Situ with Small-Period X-Ray Standing Waves. J. Colloid Interface Sci. 225, 154–165. doi:10.1006/jcis.2000.6756

Feyer, V., Plekan, O., Šutara, F., Cháb, V., Matolín, V., Prince, K.C., 2011. Guanine adsorption on the Cu(110) surface. Surf. Sci. 605, 361–365. doi:10.1016/j.susc.2010.11.002

Francis, S.H., Corbin, J.D., 1999. Cyclic Nucleotide-Dependent Protein Kinases: Intracellular Receptors for cAMP and cGMP Action. Crit. Rev. Clin. Lab. Sci. 36, 275–328. doi:10.1080/10408369991239213

Gao, B., Liu, Z., 2005. First Principles Study on the Solvation and Structure of $C_2O_4^{2-}$ $(H_2O)_n$, $n= 6$-12. J. Phys. Chem. A 109, 9104–9111.

Hassanali, A.A., Zhang, H., Knight, C., Shin, Y.K., Singer, S.J., 2010. The Dissociated Amorphous Silica Surface: Model Development and Evaluation. J. Chem. Theory Comput. 6, 3456–3471. doi:10.1021/ct100260z

Heyrovský, M., 2005. Catalytic Hydrogen Evolution at Mercury Electrodes from Solutions of Peptides and Proteins, in: Emil Paleček, F.S. and J.W. (Ed.), Perspectives in Bioanalysis, Electrochemistry of Nucleic Acids and Proteins – Towards Electrochemical Sensors for Genomics and Proteomics. Elsevier, pp. 657–687.

Ho, T.A., Striolo, A., 2013. Polarizability effects in molecular dynamics simulations of the graphene-water interface. J. Chem. Phys. 138, 54117. doi:10.1063/1.4789583

Hodge, R., 2009. The Molecules of Life: DNA, RNA, and Proteins. Infobase Publishing.

Hoefling, M., Iori, F., Corni, S., Gottschalk, K.-E., 2010. Interaction of Amino Acids with the Au(111) Surface: Adsorption Free Energies from Molecular Dynamics Simulations. Langmuir 26, 8347–8351. doi:doi: 10.1021/la904765u

Hummer, G., Rasaiah, J.C., Noworyta, J.P., 2001. Water conduction through the hydrophobic channel of a carbon nanotube. Nature 414, 188–190. doi:10.1038/35102535

Iori, F., Di Felice, R., Molinari, E., Corni, S., 2009. GolP: An atomistic force-field to describe the interaction of proteins with Au(111) surfaces in water. J. Comput. Chem. 30, 1465–1476. doi:10.1002/jcc.21165

Jedlovszky, P., Předota, M., Nezbeda, I., 2006. Hydration of apolar solutes of varying size: a systematic study. Mol. Phys. 104, 2465–2476. doi:10.1080/00268970600761101

Johnson, R.R., Kohlmeyer, A., Johnson, A.T.C., Klein, M.L., 2009. Free Energy Landscape of a DNA-Carbon Nanotube Hybrid Using Replica Exchange Molecular Dynamics. Nano Lett. 9, 537–541. doi:doi: 10.1021/nl802645d

Jordheim, L.P., Durantel, D., Zoulim, F., Dumontet, C., 2013. Advances in the development of nucleoside and nucleotide analogues for cancer and viral diseases. Nat. Rev. Drug Discov. 12, 447–464. doi:10.1038/nrd4010

Kawamura, K., Ikushima, K., 1993. Seasonal changes in the distribution of dicarboxylic acids in the urban atmosphere. Environ. Sci. Technol. 27, 2227–2235. doi:10.1021/es00047a033

Kundu, J., Neumann, O., Janesko, B.G., Zhang, D., Lal, S., Barhoumi, A., Scuseria, G.E., Halas, N.J., 2009. Adenine− and Adenosine Monophosphate (AMP)−Gold Binding Interactions Studied by Surface-Enhanced Raman and Infrared Spectroscopies. J Phys Chem C 113, 14390–14397. doi:10.1021/jp903126f

Kuss, J., Holzmann, J., Ludwig, R., 2009. An elemental mercury diffusion coefficient for natural waters determined by molecular dynamics simulation. Environ. Sci. Technol. 43, 3183–3186.

Langmuir, I., 1918. THE ADSORPTION OF GASES ON PLANE SURFACES OF GLASS, MICA AND PLATINUM. J. Am. Chem. Soc. 40, 1361–1403. doi:10.1021/ja02242a004

Leach, A., 2001. Molecular Modelling: Principles and Applications (2nd Edition). Prentice Hall.

Leontyev, I.V., Stuchebrukhov, A.A., 2012. Polarizable Mean-Field Model of Water for Biological Simulations with AMBER and CHARMM Force Fields. J. Chem. Theory Comput. 8, 3207–3216. doi:10.1021/ct300011h

Li, X., Yi Kuang, Shi, J., Gao, Y., Lin, H.-C., Xu, B., 2011. Multifunctional, Biocompatible Supramolecular Hydrogelators Consist Only of Nucleobase, Amino Acid, and Glycoside. J Am Chem Soc 133, 17513–17518. doi:10.1021/ja208456k

Lim, J.K., Kim, Y., Lee, S.Y., Joo, S.-W., 2008. Spectroscopic analysis of l-histidine adsorbed on gold and silver nanoparticle surfaces investigated by surface-enhanced Raman scattering. Spectrochim. Acta. A. Mol. Biomol. Spectrosc. 69, 286–289. doi:10.1016/j.saa.2007.05.007

Lu, G., Maragakis, P., Kaxiras, E., 2005. Carbon Nanotube Interaction with DNA. Nano Lett. 5, 897–900. doi:10.1021/nl050354u

Luan, B., Huynh, T., Zhou, R., 2015. Simplified TiO2 force fields for studies of its interaction with biomolecules. J. Chem. Phys. 142, 234102. doi:10.1063/1.4922618

Maleki, A., Alavi, S., Najafi, B., 2011. Molecular Dynamics Simulation Study of Adsorption and Patterning of DNA Bases on the Au(111) Surface. J Phys Chem C 115, 22484–22494. doi:10.1021/jp207533p

Marrubini, G., Mendoza, B.E.C., Massolini, G., 2010. Separation of purine and pyrimidine bases and nucleosides by hydrophilic interaction chromatography. J. Sep. Sci. 33, 803–816. doi:10.1002/jssc.200900672

Matsui, M., Akaogi, M., 1991. Molecular Dynamics Simulation of the Structural and Physical Properties of the Four Polymorphs of TiO2. Mol. Simul. 6, 239–244. doi:10.1080/08927029108022432

Mignon, P., Ugliengo, P., Sodupe, M., 2009. Theoretical Study of the Adsorption of RNA/DNA Bases on the External Surfaces of Na+-Montmorillonite. J Phys Chem C 113, 13741–13749. doi:10.1021/jp901699q

Monti, S., Walsh, T.R., 2011. Molecular Dynamics Simulations of the Adsorption and Dynamical Behavior of Single DNA Components on TiO2. J Phys Chem C 115, 24238–24246. doi:10.1021/jp207950p

Munro, L.J., Johnson, J.K., Jordan, K.D., 2001. An interatomic potential for mercury dimer. J. Chem. Phys. 114, 5545. doi:10.1063/1.1351877

Pagliai, M., Caporali, S., Muniz-Miranda, M., Pratesi, G., Schettino, V., 2012. SERS, XPS, and DFT Study of Adenine Adsorption on Silver and Gold Surfaces. J Phys Chem Lett 3, 242–245. doi:10.1021/jz201526v

Paleček, E., Bartošík, M., 2012. Electrochemistry of Nucleic Acids. Chem. Rev. 112, 3427–3481. doi:10.1021/cr200303p

Paleček, E., Černocká, H., Ostatná, V., Navrátilová, L., Brázdová, M., 2014. Electrochemical sensing of tumor suppressor protein p53–deoxyribonucleic acid complex stability at an electrified interface. Anal. Chim. Acta 828, 1–8. doi:10.1016/j.aca.2014.03.029

Paleček, E., Tkáč, J., Bartošík, M., Bertók, T., Ostatná, V., Paleček, J., 2015. Electrochemistry of Nonconjugated Proteins and Glycoproteins. Toward Sensors for Biomedicine and Glycomics. Chem. Rev. 115, 2045–2108. doi:10.1021/cr500279h

Panigrahi, S., Bhattacharya, A., Banerjee, S., Bhattacharyya, D., 2012. Interaction of Nucleobases with Wrinkled Graphene Surface: Dispersion Corrected DFT and AFM Studies. J Phys Chem C 116, 4374–4379. doi:10.1021/jp207588s

Piana, S., Bilic, A., 2006. The Nature of the Adsorption of Nucleobases on the Gold [111] Surface. J. Phys. Chem. B 110, 23467–23471. doi:10.1021/jp064438i

Plekan, O., Feyer, V., Ptasińska, S., Tsud, N., Cháb, V., Matolín, V., Prince, K.C., 2010. Photoemission Study of Thymidine Adsorbed on Au(111) and Cu(110). J. Phys. Chem. C 100812144836018. doi:10.1021/jp105341k

Plekan, O., Feyer, V., Šutara, F., Skála, T., Švec, M., Cháb, V., Matolín, V., Prince, K.C., 2007. The adsorption of adenine on mineral surfaces: Iron pyrite and silicon dioxide. Surf. Sci. 601, 1973–1980. doi:10.1016/j.susc.2007.02.032

Plekan, O., Feyer, V., Tsud, N., Vondráček, M., Cháb, V., Matolín, V., Prince, K.C., 2012. Adsorption of 5-halouracils on Au(111). Surf. Sci. 606, 435–443. doi:10.1016/j.susc.2011.11.002

Porter, J.D., Zinn, A.S., 1993. Ordering of liquid water at metal surfaces in tunnel junction devices. J. Phys. Chem. 97, 1190–1203. doi:10.1021/j100108a015

Předota, M., Bandura, A.V., Cummings, P.T., Kubicki, J.D., Wesolowski, D.J., Chialvo, A.A., Machesky, M.L., 2004a. Electric Double Layer at the Rutile (110) Surface. 1. Structure of Surfaces and Interfacial Water from Molecular Dynamics by Use of ab Initio Potentials. J Phys Chem B 108, 12049–12060. doi:10.1021/jp037197c

Předota, M., Cummings, P.T., Wesolowski, D.J., 2007. Electric Double Layer at the Rutile (110) Surface. 3. Inhomogeneous Viscosity and Diffusivity Measurement by Computer Simulations. J Phys Chem C 111, 3071–3079. doi:10.1021/jp065165u

Předota, M., Machesky, M.L., Wesolowski, D.J., Cummings, P.T., 2013. Electric Double Layer at the Rutile (110) Surface. 4. Effect of Temperature and pH on the Adsorption and Dynamics of Ions. J. Phys. Chem. C 117, 22852–22866. doi:10.1021/jp407124p

Předota, M., Zhang, Z., Fenter, P., Wesolowski, D.J., Cummings, P.T., 2004b. Electric Double Layer at the Rutile (110) Surface. 2. Adsorption of Ions from Molecular Dynamics and X-ray Experiments. J Phys Chem B 108, 12061–12072. doi:10.1021/jp037199x

Rajarajeswari, M., Iyakutti, K., Kawazoe, Y., 2011. Adsorption mechanism of single guanine and thymine on single-walled carbon nanotubes. J. Mol. Model. 17, 2773–2780. doi:10.1007/s00894-010-0946-7

Rapino, S., Zerbetto, F., 2005. Modeling the Stability and the Motion of DNA Nucleobases on the Gold Surface. Langmuir 21, 2512–2518. doi:10.1021/la047091o

Ridley, M.K., n.d. personal communication.

Rosas-García, V.M., del Carmen Sáenz-Tavera, I., Rodríguez-Herrera, V.J., Garza-Campos, B.R., 2013. Microsolvation and hydration enthalpies of $CaC_2O_4(H_2O)$ n (n=0-16) and $C_2O_4^{2-}(H_2O)$ n (n=0-14): an ab initio study. J. Mol. Model. 19, 1459–1471. doi:10.1007/s00894-012-1707-6

Sanghvi, Y.S., Guo, Z., Pfundheller, H.M., Converso, A., 2000. Improved Process for the Preparation of Nucleosidic Phosphoramidites Using a Safer and Cheaper Activator. Org Process Res Dev 4, 175–181. doi:10.1021/op990086k

Schlick, T., 2002. Molecular Modeling and Simulation: An Interdisciplinary Guide. Springer-Verlag New York, Inc., Secaucus, NJ, USA.

Sestáková, I., Mader, P., 2000. Voltammetry on mercury and carbon electrodes as a tool for studies of metallothionein interactions with metal ions. Cell. Mol. Biol. Noisy--Gd. Fr. 46, 257–267.

Sharma, S., Nath, R., Thind, S.K., 1993. Recent advances in measurement of oxalate in biological materials. Scanning Microsc. 7, 431–441.

Słojkowska, R., Jurkiewicz-Herbich, M., 1999. Adsorption of L-histidine from aqueous solutions on the mercury electrode and air/solution interface. Pol. J. Chem. 73 nr 3, 527–539.

Sowerby, S.J., Cohn, C.A., Heckl, W.M., Holm, N.G., 2001. Differential adsorption of nucleic acid bases: Relevance to the origin of life. Proc. Natl. Acad. Sci. U. S. A. 98, 820–822.

Umadevi, D., Sastry, G.N., 2011. Quantum Mechanical Study of Physisorption of Nucleobases on Carbon Materials: Graphene versus Carbon Nanotubes. J Phys Chem Lett 2, 1572–1576. doi:10.1021/jz200705w

Vainrub, A., Pettitt, B.M., 2003. Sensitive Quantitative Nucleic Acid Detection Using Oligonucleotide Microarrays. J. Am. Chem. Soc. 125, 7798–7799. doi:doi:10.1021/ja035020q

Varghese, N., Mogera, U., Govindaraj, A., Das, A., Maiti, P.K., Sood, A.K., Rao, C.N.R., 2009. Binding of DNA Nucleobases and Nucleosides with Graphene. ChemPhysChem 10, 206–210. doi:10.1002/cphc.200800459

Vidossich, P., Lledós, A., Ujaque, G., 2016. First-Principles Molecular Dynamics Studies of Organometallic Complexes and Homogeneous Catalytic Processes. Acc. Chem. Res. doi:10.1021/acs.accounts.6b00054

Yang, B., Wang, Y., Li, G., Cun, H., Ma, Y., Du, S., Xu, M., Song, Y., Gao, H.-J., 2009. Influence of Deoxyribose Group on Self-Assembly of Thymidine on Au(111). J Phys Chem C 113, 17590–17594. doi:10.1021/jp906944c

Zhang, Z., Fenter, P., Cheng, L., Sturchio, N.C., Bedzyk, M.J., Předota, M., Bandura, A., Kubicki, J.D., Lvov, S.N., Cummings, P.T., Chialvo, A.A., Ridley, M.K., Bénézeth, P., Anovitz, L., Palmer, D.A., Machesky, M.L., Wesolowski, D.J., 2004. Ion Adsorption at the Rutile Water Interface: Linking Molecular and Macroscopic Properties. Langmuir 20, 4954–4969. doi:10.1021/la0353834

Zhao, Payne, C.M., Cummings, P.T., 2007. Controlled Translocation of DNA Segments through Nanoelectrode Gaps from Molecular Dynamics. J Phys Chem C 112, 8–12. doi:10.1021/jp709652y

Zheng, M., Jagota, A., Semke, E.D., Diner, B.A., Mclean, R.S., Lustig, S.R., Richardson, R.E., Tassi, N.G., 2003. DNA-assisted dispersion and separation of carbon nanotubes. Nat Mater 2, 338–342. doi:10.1038/nmat877

Zhou, H., Ganesh, P., Presser, V., Wander, M.C.F., Fenter, P., Kent, P.R.C., Jiang, D., Chialvo, A.A., McDonough, J., Shuford, K.L., Gogotsi, Y., 2012. Understanding controls on interfacial wetting at epitaxial graphene: Experiment and theory. Phys. Rev. B 85, 35406. doi:10.1103/PhysRevB.85.035406

Zuman, P., Paleček, E., 2005. Polarography of Proteins: A History, in: Emil Paleček, F.S. and J.W. (Ed.), Perspectives in Bioanalysis, Electrochemistry of Nucleic Acids and Proteins – Towards Electrochemical Sensors for Genomics and Proteomics. Elsevier, pp. 755–771.

[OK1]

Kroutil O., Chval Z., Skelton A. A., Předota M.

Computer Simulations of Quartz (101)–Water Interface over a Range of pH Values

Participation of Ondřej Kroutil:

OK implemented new force field to Gromacs software package, performed all molecular dynamics simulations of water and ions interacting with the quartz surface and carried out all analyses. He participated in the paper writing.

ABSTRACT: The original force field for clay materials (ClayFF) developed by Cygan et al. (J. Phys. Chem. B 2004, 108, 1255) is modified to describe negative charging of the quartz (101) surface above its point of zero charge (pH ~ 2~4~0.5). The modified force field adopts the scaled natural bond orbital charges derived by the quantum mechanical calculations which are used to obtain the desired surface charge density and to determine the delocalization of the charge after deprotonation of surface silanol groups. Classical molecular dynamics simulations (CMD) of the (101) surface of α-quartz with different surface charge densities (0, −0.03, −0.06, and −0.12 C.m^{-2}) are performed to evaluate the influence of the negative surface charge on interfacial water and adsorption of Na^{+}, Rb^{+}, and Sr^{2+} ions. The CMD results are compared with ab initio calculations, X-ray experiment, and the triple-layer model. The modified force field can be easily implemented in common molecular dynamics packages and used for simulations of interactions between quartz surfaces and various (bio)molecules over a wide range of pH values.

[OK2]

Kabeláč M., **Kroutil O.**, Předota M., Lankaš F., Šíp M.

Influence of a charged graphene surface on the orientation and conformation of covalently attached oligonucleotides: a molecular dynamics study

Physical Chemistry Chemical Physics 14 (12), 4217-4229, (2012)

[IF(2014) = 4.493]

Participation of Ondřej Kroutil:

OK prepared the model of graphene and attached oligonucleotide, performed several molecular dynamics simulations and participated in the paper writing.

ABSTRACT: Molecular dynamics (MD) simulations of single-stranded (ss) and double-stranded (ds) oligonucleotides anchored *via* an aliphatic linker to a graphene surface were performed in order to investigate the role of the surface charge density in the structure and orientation of attached DNA. Two types of interactions of DNA with the surface are crucial for the stabilisation of the DNA–surface system. Whereas for a surface with a zero or low positive charge density the dispersion forces between the base(s) and the surface dominate, the higher charge densities applied on the surface lead to a strong electrostatic interaction between the phosphate groups of DNA, the surface and the ions. At high-charge densities, the interaction of the DNA with the surface is strongly affected by the formation of a low-mobility layer of counterions compensating for the charge of the surface. A considerable difference in the behaviour of the ds-DNA and ss-DNA anchored to the layer was observed. The ds-DNA interacts with the surface at low- and zero-charge densities exclusively by the nearest base pair. It keeps its geometry close to the canonical B-DNA form, even at surfaces with high-charge densities. The ss-DNA, owing to its much higher flexibility, has a tendency to maximise the attraction to the surface exploiting more bases for the interaction. The interaction of the polar amino group(s) of the base(s) of ss-DNA with a negatively charged surface also contributes significantly to the system stability.

[OK3]

Dorčák V., Kabeláč M., **Kroutil O.**, Bednářová K. and Vacek J.

Electrocatalytic Monitoring of Peptidic Proton-Wires

Participation of Ondřej Kroutil:

OK participated in the paper writing.

ABSTRACT: The transfer of protons or proton donor/acceptor abilities are important phenomena in many biomolecular systems. One example is the recently proposed peptidic proton-wires (H-wires), but the ability of these His-containing peptides to transfer protons has only been studied at the theoretical level so far. Here, for the first time the proton transfer ability of peptidic H-wires is characterized experimentally in an adsorbed state using an approach based on a label-free electrocatalytic reaction. The experimental findings are complemented by theoretical calculations at the *ab initio* level in a vacuum and implicit solvent. Experimental and theoretical results indicated $Ala_3(His\text{-}Ala_2)_6$ to be a high proton-affinity peptidic H-wire model. The metodology presented here could be used for the further investigation of the proton-exchange chemistry of other biologically or technologically important macromolecules.

[OK4]

Kroutil O., Minofar B. and Kabeláč M.

Structure and Dynamics of Solvated Hydrogenoxalate and Oxalate Anions: a Theoretical Study

Manuscript

Participation of Ondřej Kroutil:

OK prepared all models, performed all ab initio molecular dynamics simulations and did several analyses. He participated in the paper writing.

ABSTRACT: Hydrogenoxalate (charge -1) and oxalate (charge -2) anions and their solvated forms were studied by various computational techniques. Ab initio quantum chemical calculations in gas phase, in implicit solvent and microsolvated (up to 32 water molecules) environment were performed in order to explore a potential energy surface of both anions. The solvation envelope of water molecules around them and the role of water on the conformation of the anions was revealed by means of Born–Oppenheimer molecular dynamics simulations and optimization procedures. The structure of the anions was found to be dependent on the number of water molecules in the solvation shell. A subtle interplay between intramolecular and intermolecular hydrogen bonding dictates the final conformation and thus an explicit solvent model is necessary for a proper description of this phenomena.